Open access • Journal Article • DOI:10.1029/JC075I030P05831

The infrared interferometer experiment on Nimbus 3 — Source link

Barney J. Conrath, Rudolf A. Hanel, Virgil G. Kunde, C. Prabhakara

Institutions: Goddard Space Flight Center

Published on: 20 Oct 1970 - Journal of Geophysical Research (John Wiley & Sons, Ltd)

Topics: Michelson interferometer, Interferometry and Astronomical interferometer

X-620-70-213

PREPRINT

NASA TM X- 63953

THE INFRARED INTERFEROMETER EXPERIMENT ON NIMBUS 3

B.J. CONRATH
R.A. HANEL
V.G. KUNDE
C. PRABHAKARA

JUNE 1970

GODDARD SPACE FLIGHT CENTER
GREENBELT, MARYLAND

X-620-70-213

PREPRINT

THE INFRARED INTERFEROMETER EXPERIMENT ON NIMBUS 3

B. J. Conrath

R. A. Hanel

V. G. Kunde

C. Prabhakara

June 1970

GODDARD SPACE FLIGHT CENTER

Greenbelt, Maryland

THE INFRARED INTERFEROMETER EXPERIMENT ON NIMBUS 3

B. J. Conrath

R. A. Hanel

V. G. Kunde

C. Prabhakara

ABSTRACT

The Michelson interferometer experiment carried on the Nimbus 3 satellite has successfully obtained thermal emission spectra of the earth and atmosphere between 400 cm^{-1} and 2000 cm^{-1} with a resolution equivalent to 5 cm^{-1}. Comparison of a measured spectrum with a spectrum calculated theoretically from near-simultaneous radiosonde measurements indicates generally good agreement over most of the spectral range covered. A preliminary search for spectral features due to minor atmospheric constituents other than CO_2, H_2O, and O_3 has resulted in a positive identification of only CH_4 thus far. Comparisons of temperature profiles estimated from selected spectra with those obtained from radiosonde measurements on both an individual basis and in the form of maps for selected locations and times indicate that meaningful atmospheric temperatures can be obtained, even in the presence of clouds. Similar comparisons of water vapor estimates with radiosonde measurements demonstrate that good humidity profiles can be obtained under essentially clear sky conditions, but when clouds

are present within the field-of-view, the estimates become unreliable. Total ozone amounts in an atmospheric column obtained from the spectra are in generally good agreement with Dobson spectrometer measurements, and the estimates are found to be insensitive to clouds within the field-of-view under most circumstances. A global map of ozone, constructed from data taken over a 24-hour period, shows anticipated correlations with a conventional 300 mb pressure height map in the Northern Hemisphere. The possibility of obtaining information on surface composition is investigated, using a spectrum obtained over Egypt which shows a depression of as much as 10°K in brightness temperature in portions of the atmospheric window. This effect can be attributed to restrahlen due to the presence of SiO_2 in the desert soil.

CONTENTS

THE INFRARED INTERFEROMETER EXPERIMENT ON NIMBUS 3

I. INTRODUCTION

During the first decade of satellite meteorology the mapping of cloud patterns and radiometric measurements in relatively broad spectral intervals accounted for nearly all the information gathered for research and operational purposes. Cloud patterns have been observed, day and night, from low altitudes, as well as from geostationary altitudes, and with a variety of spatial resolution elements. The positions and motions of frontal systems and storms are now routinely derived from cloud pictures. Several radiometers sensitive in the visible and many with channels sensitive in the infrared have been used to infer the radiation budget of local regions, surface and mean stratospheric temperatures, moisture patterns and surface related parameters. A recent survey is given, for example, by Möller and Raschke, 1969.

With the launch of Nimbus 3 on April 14, 1969, a new chapter was begun on the use of satellite-borne sensors for atmospheric research. The vertical sounding of several atmospheric parameters has now become a reality (Wark and Hilleary, 1969; Hanel and Conrath, 1969). On a global basis, profiles of temperature, humidity, and ozone may now be derived by interpretation of the thermal emission spectrum. The infrared interferometer flown on Nimbus 3 has provided thermal emission spectra from 400 cm^{-1} to 2000 cm^{-1} (5–25μm) with apodized

resolution elements of 5 cm^{-1}. By spectroscopic standards this resolution is still low, only the contours of the 667 cm^{-1} (15μ m) CO_2 band are resolved, but the spectral resolution is adequate for many purposes, and combined with the good radiometric accuracy of the instrument, many new avenues of research have now become possible.

The 667 cm^{-1} CO_2 band is available for estimating temperature profiles and the 1042 cm^{-1} (9.6μm) ozone band, as well as portions of the rotation, and 1595 cm^{-1} (6.3μm) water vapor bands may be analyzed to yield information on the vertical distribution and total amount of ozone and water vapor. The semi-transparent window regions in the 800-1250 cm^{-1} (8-12.5μm) spectral interval permit studies relating to remote sensing of surface features, such as a search for reststrahlen phenomena. The spectra, combined with in situ radiosonde measurements of temperature and water vapor, provide an opportunity of testing gaseous transmittance theory under conditions of pressure and path length which cannot be obtained in the laboratory.

In this paper, after a brief description of the instrument, comparisons of measured and calculated spectra are given, and problem areas in the theory of atmospheric transmittances are pointed out. After having gained confidence in the measurements, temperature and water vapor estimation techniques are applied to selected spectra, and the results are compared with in situ measurements obtained from radiosondes flown at approximately the same times and locations.

Estimates of ozone total amounts and vertical distributions are compared with Dobson spectrometer measurements and in situ ozone sonde measurements. The effect of clouds within the field-of-view and other limitations to the precision of the derived quantities have been investigated, and techniques designed to overcome some of these limitations have been applied to the data. The global capabilities of such measurements are demonstrated by examples of maps showing temperature fields and global distributions of total ozone. Finally, examples of spectra are given which show reststrahlen phenomena and possible applications of such measurements are considered.

II. DESCRIPTION OF THE INSTRUMENT

The recording of a wide spectral range from approximately 400 to 2000 cm^{-1} at a relatively high spectral resolution corresponding to 5 cm^{-1} within a permitted time interval of about ten seconds is a difficult task. At the beginning of this project it seemed to be beyond the state-of-the-art to perform this measurement from a satellite since, in addition to the requirements mentioned, a radiometric precision of 1% and an accuracy approaching the same order of magnitude was estimated to be necessary to achieve the scientific objectives of this experiment. It was recognized then that the only method which could possibly reach this ambitious goal was Fourier spectroscopy using a Michelson interferometer. The multiplex and the large "solid-angle-times-area" (étendue) advantage of the Michelson interferometer had to be exploited fully to obtain the required spectral

resolution and precision while covering a wide spectral range. At the same time the required accuracy made on-board calibration of the instrument mandatory.

The advantages of the Michelson interferometer are not easily realized. This type of interferometer requires nearly perfect optical alignment, is known to be rather sensitive to external vibration, and the data channel demands a large dynamic range. Furthermore, the required radiometric precision had never been achieved before in a small instrument of this nature. Nevertheless, the IRIS-B interferometer flown on Nimbus 3 came close to theoretical expectations and has achieved set goals to a high degree. In orbit this instrument performed well, although not flawlessly. The equilibrium temperature was about 5°K higher than the desired 250°K, and some misalignment made the 1400-2000 cm^{-1} (5-7 μm) range unreliable after approximately 50 orbits.

A brief description of the interferometer and its use as a spectral analyzer will be given here. A more detailed analysis of the instrument and a discussion of its performance is published elsewhere (Hanel, et al., 1970). The main elements of the Michelson interferometer, as shown in Figure 1, are the beamsplitter, the fixed mirror, and the moving mirror, often called the Michelson mirror. Figure 2 shows the external configuration of the instrument. The amplitude of the incoming radiation is divided by the beamsplitter into two approximately equal components. After reflection on the fixed and moving mirrors respectively, these components interfere with each other with a phase corresponding to the difference in the optical path between the beams. The intensity, i, of

the recombined beams is recorded by the thermistor bolometer as a function of the optical path difference, δ. The signal, called the interferogram, is the auto-correlation function of the incoming net radiation, and, neglecting constant terms, can be expressed in the form

$$i(\delta) = \int r(\nu) \left[I(\nu) - I_i(\nu)\right] \cos\left[2\pi\nu\delta - \phi(\nu)\right] d\nu \qquad (1)$$

In this equation $r(\nu)$ is the spectral responsivity, $I(\nu)$ and $I_i(\nu)$ are the radiance of the scene and the instrument respectively, ν is the wave number in cm^{-1} and $\phi(\nu)$ is a phase angle. The goal of the data reduction is to recover the spectral radiance of the scene in absolute radiometric units. The interferogram is amplified, limited in bandwidth by an electrical filter, and quantized by an analog-to-digital converter. The sample command for the analog-to-digital conversion is derived from an auxiliary or fringe control interferometer which is coaxial with the main interferometer and, in effect, measures the mirror displacement very accurately. The fringe control interferometer provides a precise wave number scale for the measured infrared spectrum. The 0.5852 μm line of a neon discharge source is used as the standard. The velocity of the Michelson mirror is controlled by a feedback circuit which slaves the mirror motion to a stable spacecraft clock frequency. The phase-locked-loop operation of the Michelson mirror has contributed considerably to the quality of the spectra.

The required radiometric accuracy was achieved by an on-board calibration technique. After recording 14 interferograms while viewing earth, the 15th and

16th interferograms are recorded while viewing two standard sources. One standard source is a blackbody built into the instrument. The second standard is the interstellar background with a temperature of a few degrees Kelvin, which is taken as a perfect radiation sink. The temperature of the warm blackbody is carefully monitored. In the calibration process the earth spectra are scaled to the spectra from both radiation standards. It is important to note that the very first optical surface, the flat mirror mounted at 45° to the entrance port of the interferometer, as shown in Figure 1, serves as a switch for feeding the radiation standards and the source to be measured into the interferometer. Corrections due to possible changing reflectivities of other surfaces are completely avoided.

The calibration standards are measured about twenty times per orbit, and from these measurements the average orbital responsivity of the instrument is calculated. From the standard deviation of the responsivity calculated from individual calibration pairs within one orbit, the noise equivalent radiance may be determined. It can reasonably be assumed that the noise properties of the instrument are the same while viewing earth and the calibration sources, and this provides a convenient and objective assessment of the probable error of the measurement. The details of the calibration technique have been described also in the Nimbus 3 User's Guide.

The same flat mirror which permits in-flight calibration of the whole instrument also provides image motion compensation. For that purpose this mirror is rotated slowly at about 0.4 degrees per second. The 8 degree field-of-view of

the instrument points about 2° ahead along the subsatellite track at the beginning of an interferogram. At the end of the interferogram ten seconds later, the field-of-view is directed about 2° behind the subsatellite point. Therefore, the radiation which gives rise to a single interferogram originates from a well-defined circular area on earth 150 km in diameter, and smear caused by the motion of the satellite is eliminated. During the time the Michelson mirror moves back to the start position ready to record the next interferogram, the image motion compensation mirror moves to the "2° ahead" position again ready for the next measurement. The image motion compensation is inhibited during the recording of calibration interferograms. In the absence of compensation, the beginning of an interferogram may be generated by radiation originating in a cloud-free area, while the end may represent a heavily clouded case.

III. DATA PROCESSING

In the data reduction procedure the output signal of the detector, after being quantized, stored in the spacecraft tape recorder, and transmitted to the ground, is then processed in a digital computer. First, an apodization or weighting function is applied to the interferogram to reduce side lobes in the instrument function. Then the weighted interferogram is Fourier transformed to yield an amplitude and a phase spectrum. The amplitudes are proportional to the net spectral radiance between the instrument and the scene within the field-of-view. The phase spectrum is used to resolve the ambiguity in the amplitude spectrum which is created by operating the instrument at the mid-range of expected brightness

temperature. With the power spectrum alone one cannot distinguish between scenes warmer or colder than the instrument. The application of the phase spectrum to the raw power spectrum has been illustrated in the instrument paper (Hanel, et al., 1970). After the raw power spectrum has been phase corrected, the calibration process takes place.

Each uncalibrated atmospheric spectrum is scaled to the spectra from the known hot and cold calibration sources for each wave number interval. The Fourier transformation and calibration process takes approximately 0.9 second per spectrum on an IBM 360/91 computer. As mentioned before, the computation process also generates the orbital means of the responsivity of the instrument derived from the calibration spectra and the noise equivalent radiance of the instrument derived from the standard deviation of the individual blackbody spectra. Samples of these quantities are shown in Figure 3.

By the calibration process the desired quantity, the radiance of the observed scene, averaged over the field-of-view, is obtained in absolute radiometric units, erg sec^{-1} cm^{-1} $ster^{-1}$, within the limitations of spectral resolution and precision of the instrument. The spectral resolution is verified by comparison of spectra calculated with a resolution of 5 cm^{-1} and the precision is estimated from the repeatability of the calibration spectra.

IV. THE THERMAL EMISSION SPECTRUM

In the thermal infrared the emergent radiance of a planetary atmosphere depends on atmospheric emission, absorption, and scattering processes as well

as on the emission and reflection properties of the surface below. Neglecting scattering, the spectral radiance as measured at the satellite, may be expressed as

$$I(\nu) = \epsilon^s(\nu)\, B(\nu, T_s)\, \tau^s(\nu) + \left[1 - \epsilon^s(\nu)\right] F^{\downarrow}(\nu)\, \tau^s(\nu) + \int_{\tau^s(\nu)}^{1} B(\nu, T)\, d\tau(\nu) \tag{2}$$

The first term on the right hand side of equation (2) represents radiation emitted by the surface at temperature T_s having an emissivity $\epsilon^s(\nu)$. $B(\nu, T_s)$ is the Planck function at wave number ν and temperature T_s and $\tau^s(\nu)$ is the atmospheric transmission at the surface. The second term represents the downward atmospheric flux, $F^{\downarrow}(\nu)$, diffusely reflected by the surface; the reflectivity is taken as one minus the emissivity and a Lambertian reflection law is assumed. Most natural surfaces on earth have a high emissivity, close to that of a blackbody so the second term can frequently be neglected. However, this is not always true when certain minerals are exposed, such as in desert areas. This term is also significant in the microwave region of the spectrum where it must be taken into consideration. The last term in equation (2), accounting for direct emission by the atmosphere, is the most important one for vertical sounding.

The monochromatic transmittance between geometric levels s' and s'' is given by

$$\tau(\nu) = \exp\left[-\int_{s''}^{s'} \sum_i k_i(\nu, P, T)\, \rho_i\, ds\right] \tag{3}$$

where the total molecular line absorption coefficient of the i^{th} constituent is k_i, and the gas density of the constituent is ρ_i.

The theory of remote sensing is based on a measurement of selected values of $I(\nu)$. The field-of-view of IRIS (4° half angle) is narrow enough so the measured quantity may be regarded as the radiance in the vertical even though in reality radiances up to 4° from the vertical contribute to a spectrum. As mentioned above, the second term of equation (2) can often be neglected, $\left[1-\epsilon^s(\nu)\right]<<1$, allowing the transfer equation to be written as

$$I(\nu) = \epsilon^s(\nu).B\left(\nu, T_s\right)\ \tau^s(\nu) + \int_{\tau^s(\nu)}^{1} B(\nu, T)\ d\tau(\nu) \quad , \quad (4)$$

Surface phenomena may be determined from the emergent spectrum in atmospheric "window" regions where the atmospheric emission term is small. If the atmospheric transmittance at the surface can be estimated, it is then possible to attempt to determine either the surface temperature or the surface emissivity for surfaces where at least one of the two parameters can be reasonably approximated. Atmospheric temperatures and composition may be determined from strongly absorbing spectral regions where the atmospheric term of equation (4) is dominant. The temperatures expressed by the Planck function may be recovered within certain limitations if the incremental atmospheric transmittances are known, as is the case for a gas of constant mixing ratio, such as CO_2. Once the temperatures are known, the incremental transmittances of other gases may be determined

in spectral regions where the gases dominate, allowing their concentrations to be found. All these methods will be explored below, but before this can be done, atmospheric transmittances have to be verified, and assumptions, such as the neglect of scattering processes in the clear atmosphere, have to be shown to be justified.

In many cases absorption coefficients of gases are determined in laboratory tests with generally short path lengths and it is often problematic to extrapolate these measurements to atmospheric conditions of long path length, as well as variable pressure and temperature. Nevertheless, it is instructive and necessary to predict the radiance values for a particular case using the best presently available transmittance parameters and radiosonde data for temperatures and humidities applicable to the case.

V. COMPARISON OF MEASURED AND CALCULATED SPECTRA

The comparison of measured and theoretically predicted spectra aid in the analysis of the data and also serve to validate the instrumental performance, both in a spectral sense, and to a lesser degree, in a radiometric sense. The monochromatic spectrum of equation (4) is smoothed by the finite spectral resolution of the instrument. The observed spectrum $\bar{I}(\nu)$ is the convolution of the true spectrum with the instrument function,

$$\bar{I}(\nu) = \int_{\nu - a}^{\nu + a} f\left(|\nu' - \nu|, a\right) I(\nu')\, d\nu' \Big/ \int_{\nu - a}^{\nu + a} f\left(|\nu' - a, a\right) d\nu' \quad (5)$$

where "a" represents the width of the instrument function at half maximum. For radiance computations, the instrument function of IRIS can be satisfactorily represented by a triangular function with a = 5 cm^{-1}.

The total monochromatic absorption coefficient for the i^{th} species may be written as

$$k_i(\nu, P, T) = k_i^d(\nu, P, T) + k_i^\circ(\nu, T) \frac{P_e}{P_o} \quad (6)$$

The above expression results from considering the monochromatic absorption coefficient for each line for distances less than and greater than a distance D from the line center in terms of a direct and wing contribution respectively. The derivation of the above expression has been discussed previously (Kunde, 1968: 1969). The subscript "o" indicates reference conditions. The effective pressure, P_e, is

$$P_e = P + (B - 1)\, p \quad (7)$$

with P being the total pressure, p the partial pressure of the absorbing gas and B the self-broadening coefficient. The technique of separating each line into a direct and wing contribution has the advantage that one need consider only lines in the interval ν-D to ν+D, rather than all lines, for computing $k_i^d(\nu, P, T)$, thus insuring a considerable reduction in the amount of computer time required. A second advantage is that $k_i^\circ(\nu, T)$ may be easily adjusted for empirical fitting

to observed spectra in spectral regions where the theoretical treatment is not adequate. An example of this will be discussed later for the rotational H_2O lines in the 1000 cm^{-1} "window".

The solution of equations (4), (5) and (6) is accomplished entirely by numerical techniques which will be described elsewhere. The line data used in the calculations were those of Benedict and Kaplan (1967) for the pure rotational lines of water vapor, Benedict and Calfee (1967) for the 1595 cm^{-1} band of water vapor, Drayson and Young (1967) for the 667 cm^{-1} band of carbon dioxide and Clough and Kneizys (1965) for the 1042 and 1103 cm^{-1} bands of ozone. The line data for the 961 and 1064 cm^{-1} bands of CO_2 were computed using standard spectroscopic formulation and the band strengths of Gray (1967). The published collisional line half-widths were used for water vapor and constant line half-widths of 0.8 and 0.7 cm^{-1} were assumed for carbon dioxide and ozone, respectively. Absorption by CH_4 and N_2O in the 1250-1400 cm^{-1} region was represented by the empirical fits to low spectral resolution ($\sim$10 cm^{-1}) laboratory data made by Green and Griggs (1963). For N_2O, with a fairly uniform line spacing of $\sim$0.84 cm^{-1} (Plyer and Barker, 1931), the spectral envelope of the band is essentially the same for the 5 cm^{-1} resolution of IRIS and the 10 cm^{-1} resolution of the laboratory data. Thus, the empirical fit gives a fairly accurate spectral representation of the N_2O band. For CH_4, with the lines grouped approximately 5 cm^{-1} apart (Kyle, 1968), the empirical representation is not as accurate although it still is sufficient for a preliminary interpretation of the data.

The most difficult spectral regions for determining accurate atmospheric transmittances in a routine manner in a general algorithmic scheme are the fairly transparent "window" regions. The transmittance difficulties in "window" regions are associated with several distinct problem areas:

1) The contribution of aerosols becomes more significant because the absorption by molecules is small far away from the band centers. However, the aerosol contribution is variable depending on composition, size distribution and vertical concentration, and as these characteristics are not routinely available, along with radiosonde data, it is extremely difficult to correct for aerosol scattering. The continuum absorption coefficients derived by Bolle (1965) vary by factors up to 4 due to varying atmospheric conditions.

2) The molecular absorption contribution in "window" regions is due to the wings of the lines in the strongly absorbing bands. The state-of-the-art in determining the wing contribution is extremely uncertain as it is not possible to represent the line shape or its strong dependence on temperature and type of broadening gas in a general manner. Substantial deviations from the Lorentz line shape in the line wings have been observed in numerous homogeneous and slant path spectra for both CO_2 and H_2O (Bignell, Saiedy and Sheppard, 1963; Bolle, 1965, 1967; Burch, Gryvnak, Patty and Bartky, 1968; Burch, 1970), and

3) The transmission in "window" regions may partially be due to physical mechanisms other than aerosol scattering or molecular wing absorption. For example, it has been suggested that absorption in the 600-1000 cm^{-1} region

results partially from hydrogen bonding between a pair of water vapor molecules (Penner and Varanasi, 1967; Varanasi, Chou and Penner, 1968). This mechanism is consistent with the strong observed temperature dependence of the absorption coefficient, whereas none of the theoretical line-shapes is consistent. Theoretical work on the water vapor dimer has been done by Viktorova and Zhevakin (1967) and possible experimental verification has been obtained by Harries, Burroughs and Gebbie (1969) and Burroughs, Jones and Gebbie (1969) in the far infrared region.

In this investigation, the method used to determine slant path transmittances in "window" regions is as follows: For CO_2, O_3 and the 1595 cm^{-1} band of H_2O, the theoretically determined values of $k_i°$, based on the Lorentz line shape (L), were used. The values for the rotational lines were modified in the following manner. The theoretical values of $k_i°$ are shown in Figure 4 for various line shapes where the modified Van Vleck-Weisskopf (M-VVW) type has been described by Farmer (1967), and the remaining line shapes by Burch (1968). Continuum absorption coefficients, corrected for nearby lines, derived from measurements are also indicated in Figure 4.

A considerable fraction of the scatter in the empirical continuum coefficients in Figure 4 results from the observed data not being reduced to identical reference pressure conditions. The measurements of Bolle and of Saiedy were reduced in terms of effective pressure. Bignell, Saiedy and Sheppard reduced their coefficients in terms of total pressure by attempting to correct for self-broadening

which depends on the H_2O partial pressure. The scatter in the derived coefficients thus partially reflects differences in the H_2O partial pressure at the time and location of the observations. This is consistent with the implication from the Burch (1970) investigation that H_2O-H_2O broadening governs the H_2O continuum absorption. From Figure 4 it is evident that none of the line shapes have the proper relative shape to match the observed data. The parameter k_i° has been adjusted to yield

$$k_i^\circ\ (\nu, T) = k_i^\circ\ (\nu, T)_{M\text{-}VVW} \qquad \nu < 400\ cm^{-1} \tag{8}$$

$$k_i^\circ\ (\nu, T) = k_i^\circ\ (\nu, T)_{M\text{-}VVW}\ \exp\left[-a(\nu - 400)\right] \qquad \nu \geq 400\ cm^{-1} \tag{9}$$

where a was determined by the condition

$$k_i^\circ\ (\nu, T) = k_i^\circ\ (\nu, T)_L \qquad \nu = 1000\ cm^{-1} \tag{10}$$

From the scatter illustrated in Figure 4, this procedure is expected to give only general agreement in "window" regions and it is reasonable to assume that k_i° would have to be renormalized for each individual spectrum to obtain close agreement. In view of the above discussion, it should be emphasized that the modified k_i° is to be regarded as an empirical constant rather than justification for a modified line shape. The above treatment does not adequately cope with the strong temperature dependence of the continuum.

For the comparison of the theoretical and observed spectrum, a clear atmosphere case over the Gulf of Mexico at 1734 GMT on April 22, 1969, with supporting

radiosonde data from Brownsville, Texas at 1800 GMT, was chosen. The Gulf of Mexico case was selected in order to reduce the effects of atmospheric aerosols, boundary discontinuities and surface emissivity. Approximately three minutes later in time, at 1737 GMT, the satellite passed over land near Brownsville, Texas. From the IRIS spectrum at 1737 GMT, temperature, humidity and ozone profiles were derived, and compared with the radiosonde (for temperature and humidity only) by Hanel and Conrath (1969). The Brownsville radiosonde temperature and humidity profiles and the derived ozone profile were used for this case. The surface temperature of 298°K was obtained from an NMC North American surface chart as measured by the Nomad buoy. The geographical location at 1734 GMT was approximately 26.3°N, 96.5°W. The observed spectrum was separated about 26 minutes timewise and 100 km geographically from the radiosonde data.

The mixing ratios for CO_2, CH_4, and N_2O were taken as 314, 1.75, and 0.28 parts per million (ppm), respectively, and were assumed to be constant in altitude. The concentrations of CO_2 and especially CH_4, and N_2O are expected to depend somewhat on time of the day, geographic location and season. A summary of observed mixing ratios can be found in a report by Anding (1967). The mixing ratios adopted for CH_4 and N_2O may be considered to be representative values. The atmospheric parameters concerning the gas concentrations used in the Brownsville case are summarized in Table 1.

Table 1

Summary of Atmospheric Parameters

Gas	Mixing Ratio (ppm)	Optical Depth
Water Vapor	Variable	1.58 pr-cm
Ozone	Variable	0.36 cm-atm
Carbon Dioxide	314	253 cm-atm
Methane	1.75	1.4 cm-atm
Nitrous Oxide	0.28	0.22 cm-atm

The comparison of the predicted and observed spectrum is shown in Figure 5 with the observed spectrum representing a single observation reduced in the apodized mode. The observed spectrum has been displaced 0.2 radiance units upward for clarity in the presentation. The spectra are also shown in Figures 6 and 7 on an enlarged scale.

The observed spectral features are due to the rotational lines of H_2O, the 667 cm^{-1} CO_2 band, the 1042 and 1103 cm^{-1} O_3 band, the 1306 cm^{-1} CH_4 band and the 1595 cm^{-1} water vapor band. The 964 cm^{-1} CO_2 band is also faintly evident in the spectrum. The spectral agreement across the entire region is quite good. There are several features in the observed spectrum in the 1100 cm^{-1} region which are not indicated in the theoretical spectrum. These are considered to be due to O_3 from identification by Migeotte, et al. (1957). The theoretical molecular line parameters for O_3 used in this investigation were a first generation

set. Recently these parameters have been revised considerably and updated (Clough, 1970).

In addition to the molecular features discussed above, the following molecules and their respective absorption bands occurring in the IRIS spectral region were considered.

CH_4

The ν_4 fundamental at 1306 cm^{-1} is observed. The empirical fit used to predict CH_4 absorption does not represent the Q branch adequately, even in a spectral sense. The weaker ν_2 fundamental at 1534 cm^{-1}, normally forbidden, is masked by H_2O and occurs in a region where the signal is low.

N_2O

The N_2O bands occur at 589 cm^{-1} (ν_2), 1167 cm^{-1} ($2\nu_2$) and 1285 cm^{-1}(ν_1). The 589 cm^{-1} band does not seem to be evident although an unidentified spectral feature is present in the observed spectrum at approximately 592 cm^{-1}. The observed feature may possibly be due to the rotational H_2O line which occurs at 591.69 cm^{-1}. The 1167 cm^{-1} band does not show in the spectrum and the 1285 cm^{-1} band region is heavily masked by H_2O and CH_4.

NO_2

The NO_2 bands are at 648 cm^{-1} (ν_2), 1320 cm^{-1} (ν_1) and 1621 cm^{-1} (ν_3). These bands are all heavily masked by other molecular bands and not evident.

HNO_3, SO_2, H_2S

A cursory search was also made for the following: 1) the NHO_3 bands at 879 cm^{-1} (ν_5) and 897 cm^{-1} ($2\nu_9$); the SO_2 bands at 519 cm^{-1} (ν_2), 1151 cm^{-1} (ν_1),

and 1361 cm^{-1} (ν_3) (entirely masked by H_2O, CH_4, and N_2O); and 3) the H_2S band at 1290 cm^{-1}. None of these features were evident in the observed spectrum.

The radiometric agreement across the spectrum is 10% or better for the spectral regions below 1250 cm^{-1}. For higher wave number regions somewhat larger disagreement is found due generally to the lower instrumental signal-to-noise ratio. Several spectral regions indicate that the atmospheric model, based primarily on the radiosonde data, deviates from the real atmosphere producing the observed spectrum. The systematically lower theoretical radiances in both the P-branch and R-branch wings of the 667 cm^{-1} CO_2 band indicate that the tropospheric temperature profile of the atmospheric model is probably lower than the real temperature profile. The other prime source of error is the CO_2 molecular parameters—especially the line shape or the variation of collisional half-width with rotational number—which would give the same effect. The rotational line and 1595 cm^{-1} H_2O band region also show a systematic radiance difference which most likely is due to an incorrect tropospheric temperature profile or water vapor mixing ratio. For comparison of high spectral resolution synthetic and observed spectra, the time and spatial displacement of the radiosonde data from the appropriate atmosphere producing the observed spectrum limits the degree of quantitative radiometric agreement.

The theoretical spectrum in the 1250-1350 cm^{-1} region of absorption by CH_4 has been computed for two cases: 1) H_2O only, and 2) H_2O plus CH_4 plus N_2O. Due to the low signal-to-noise and to the handling of the theoretical CH_4 absorption, the comparison should be considered only semi-quantitative. However, the

comparison is adequate enough to reflect the significant effect of the CH_4 and N_2O absorption on the emergent spectrum. A more detailed analysis of this spectral region will be made by including the N_2O and CH_4 molecular parameters in the line-by-line computational scheme and by utilizing the Nimbus 4 IRIS data which have a higher signal-to-noise ratio in this region. This type of analysis will determine the feasibility of obtaining the global variation of CH_4 from the IRIS spectra.

For this particular comparison, the theoretical treatment of the atmospheric transmission in the 1000 cm^{-1} "window" region is adequate enough to allow inferring the actual surface temperature from the IRIS data to an accuracy of better than 1°K.

It is anticipated that the use of this "window" transmittance model will not be as accurate for atmospheric cases where there is interference by aerosols or where the atmosphere is very humid. The accuracy to which the surface temperature can be inferred for varying meteorological conditions can only be determined from analysis of more IRIS spectra. The inaccuracies in the 1000 cm^{-1} "window" transmitttances are partially offset by the emergent radiance not being highly sensitive to the value of atmospheric transmittance. Computations by Saiedy and Hilleary (1967) indicate a 10% error in $k_i°$ would lead to an error of 1°K in the computed surface temperature.

Improvements in interpreting the IRIS spectra, using line-by-line procedures, may be accomplished in several areas. First, a second generation line-by-line

numerical computational scheme, more fully optimized with respect to computing time is required to allow similar comparisons between theoretical and observed radiances to be made for a range of meteorological conditions. The molecular tape atlas also requires improved molecular parameters, ozone for example, and an extension to include the lines of CH_4 and N_2O. The forthcoming Nimbus 4 IRIS with 2.8 cm^{-1} apodized resolution affords a better chance for the observation of trace gases and pollutants.

The comparison of a measured spectrum with a predicted one is generally quite favorable. The major features and many minor features can be identified. Nevertheless, more work has to be done to make the theoretical models more representative, and better observational data, including both spectra and in situ measurements for comparison purposes are needed.

VI. ATMOSPHERIC TEMPERATURES AND HUMIDITIES

The good agreement in most spectral regions between the theoretically calculated and measured spectra discussed above helps to establish confidence in both the measurements and their theoretical understanding. Once such a verification is established, it is then possible to consider certain meteorological and geophysical applications of the data.

One of the more significant applications of remote infrared spectral measurements is the estimation of vertical profiles of atmospheric temperature and humidity. Conventionally, these parameters are obtained from in situ radiosonde measurements. The radiosonde networks are adequate for the short term

operational weather forecasting requirements in the more densely populated areas, such as the continental United States and Europe, but large parts of the earth, particularly in the Southern Hemisphere, are not extensively covered. The remote vertical sounding of the atmosphere by satellite-borne instrumentation can be expected to fill the large gaps in the existing radiosonde networks and provide a truly global coverage necessary for predictions beyond a few days. Recognizing the importance of vertical temperature measurements for meteorology, but indirectly also for aviation, agriculture and other fields, the design parameters of IRIS were chosen to permit temperature sounding of the atmosphere in the 667 cm^{-1} band of CO_2.

For purposes of examining the problem of obtaining vertical temperature profiles, it is convenient to rewrite equation (4) in the form

$$I(\nu) = B(\nu, T_s)\tau^s(\nu, P_s) + \int_{\log P_s}^{\log P_t} B[\nu, T(\log P)] \frac{\partial \tau(\nu, \log P)}{\partial \log P} \, d \log P \tag{11}$$

Here the logarithm of the atmospheric pressure has been taken as the independent height related variable, and the surface emissivity $\epsilon^s(\nu)$ has been set equal to unity. The pressure level P_t is the effective "top" of the atmosphere above which the contribution to the outgoing radiation is negligible, and P_s is the surface pressure. In the examples considered here, $P_t = 0.055$ mb has been employed.

Examination of equation (11) indicates that the atmospheric contribution to the outgoing radiance at wave number ν (given by the second term) can be regarded

as the weighted mean of the Planck radiance $B\left[\nu, T(\log P)\right]$ at each level where the weighting function is $\partial\tau(\nu, \log P)/\partial \log P)$. If one assumes that CO_2 is uniformly mixed with a known mixing ratio, it is then possible to calculate the transmittances $\tau(\nu, \log P)$ and, hence, the weighting functions for many spectral intervals within the 667 cm^{-1} band, using the line-by-line integration techniques described in the previous section. An example of such a set of weighting functions is shown in Figure 8.

An examination of Figure 8 reveals that various portions of the atmosphere are weighted differently in different spectral intervals. Thus, by making a number of measurements of the spectral radiance, ranging from the strongly absorbing band center to the weakly absorbing band wing, it is possible to recover information on the vertical distribution of atmospheric temperatures. Because of the considerable width of the weighting functions and their overlap, direct estimates of temperatures obtained from the measurements tend to be highly unstable and are sensitive to random errors in the measurements.

Since it was first pointed out that vertical temperature profiles could be obtained from remote infrared measurements (King, 1958; Kaplan, 1959), much effort has been devoted to the development of techniques by which stable, physically meaningful estimates of temperature profiles could be obtained from radiance measurements containing random noise (Wark, 1961; King, 1964; Wark and Fleming, 1966; Rodgers, 1966; Strand and Westwater, 1968; Conrath, 1968, Chahine, 1968). These techniques can be divided into two general categories,

estimation techniques which employ only the radiances measured from the satellite, and statistical estimation techniques which, in addition to the satellite measurements, employ statistical information on the behavior of atmospheric temperature profiles.

Examples of applications of a statistical estimation technique to satellite measurements have been given by Wark and Hillary (1969). In the examples considered here, a nonstatistical method, based on an iterative computational technique proposed by Chahine (1968) has been employed. In this method, the temperature profile is represented by the temperatures T_i ($i = 1, 2, \ldots M$) at M predetermined "anchor" levels in the atmosphere with a prescribed interpolation between these levels. Each anchor level is paired with a given spectral interval, and the temperature associated with that level is calculated using the algorithm

$$B\left(\nu_i, T_i^{n+1}\right) = \left[\frac{\tilde{I}\left(\nu_i\right) - B\left(\nu_i, T_s\right)\tau\left(\nu_i, P_s\right)}{I^n\left(\nu_i\right) - B\left(\nu_i, T_s\right)\tau\left(\nu_i, P_s\right)}\right] B\left(\nu_i, T_i^n\right) \quad i = 1, 2, \ldots M \quad (12)$$

where T_i^{n+1} is the $(n+1)$ st estimate of T_i, and $I^n(\nu_i)$ is the theoretical radiance from equation (11), calculated using the nth estimate of the temperature consisting of the T_i^n's interpolated between the anchor levels with a predetermined interpolation scheme. The measured radiances used in equation (12) are designated by $\tilde{I}(\nu_i)$. In order to begin the iterative procedure, a first guess at a temperature profile is required, which, in the examples considered here, was

taken as an isothermal atmosphere at 250°K. The procedure is iterated until the rms difference between the calculated and measured radiances is less than the estimated rms instrumental noise.

Once the temperature profile has been calculated, it is then possible to use measurements in the water vapor absorption bands to estimate a water vapor profile. Again, nonstatistical and statistical techniques have been developed and are described in detail elsewhere (Conrath, 1969). The nonstatistical method will be considered first. In this approach, a mathematical representation for the relative humidity profile is assumed which contains N free paramters $a_1, a_2, \ldots a_N$. When this expression is substituted into equation (11), a theoretical expression for the radiances $I(\nu; a_1, \ldots a_N)$ in terms of the free parameters results. Using Q measured radiances $I(\nu_i)$ in the water vapor absorption bands, the free parameters are evaluated by requiring that

$$\sum_{i=1}^{Q} \left[I(\nu_i) - \tilde{I}(\nu_i) \right]^2 \qquad (13)$$

be minimized. This is accomplished using a Newton-Raphson calculation. In the examples considered here, the humidity profile was represented by a single line segment specified by two parameters between the surface and 300 mb. A climatological profile was employed to account for the small contribution to the radiance above 300 mb.

The surface temperature required in equation (12) and also in the humidity estimation can be obtained in principle from the atmospheric "window" region

near 900 cm^{-1}. However, as noted in the previous section, there is some atmospheric absorption in this region, primarily due to water vapor. There is also some overlapping absorption due to water vapor in the 667 cm^{-1} CO_2 absorption band. Hence, an overall iterative scheme is required for calculating the surface temperature, the atmospheric temperature, and humidity profiles.

The method employed is shown schematically in Figure 9. A first guess is made at temperature and humidity profiles, and an estimate is made of the effective surface temperature T_s using the measurement at 900 cm^{-1}. The effective surface temperature is defined as the temperature of a blackbody producing the same spectral radiance as the actual surface. In general, the effective temperature of the surface can be different from the temperature of the air immediately above the surface, and must be treated as a separate parameter. Measurements in the 667 cm^{-1} CO_2 band are then used, along with the effective surface temperature (assumed to be constant over the spectral regions employed) and a first guess at the humidity profile, to obtain a temperature profile estimate. This temperature profile and the effective surface temperature are then employed along with measurements in the water vapor bands to obtain an estimate of the water vapor profile. The procedure is iterated until the parameters being estimated change by less than a designated amount from one iteration to the next.

Figures 10 and 11 show the results of applications of the computational scheme outlined above to selected spectra. The central frequencies and bandwidths of the spectral intervals employed are indicated in Table 2. The intervals

Table 2

Spectral Intervals Employed in Temperature and Humidity Estimates

Absorbing Gas	Central Frequency (cm^{-1})	Bandwidth (cm^{-1})
CO_2, H_2O	668	5
	675	5
	680	5
	685	5
	690	5
	695	5
	700	5
	705	5
	710	5
	760	5
Atmospheric Window H_2O, CO_2	900	40
H_2O	480	40
	1240	40
	1360	40

employed in the temperature estimation are 5 cm^{-1} wide apodized spectral resolution elements. The line-by-line calculations described above were employed to obtain CO_2 transmittances in the 667 cm^{-1} band. However, it was found

necessary to introduce small modifications into the calculated transmittances at 700 cm^{-1}, 705 cm^{-1}, and 710 cm^{-1} to bring the calculated radiances into better agreement with the measured radiances. This was accomplished by rigidly translating the curves of $\tau(\nu, \ln P)$ versus $\ln P$ along the $\ln P$ axis by appropriate amounts. The modifications in each case resulted in an increase in atmospheric transmittance above each atmospheric level.

The need to recalculate the water vapor transmittances frequently made the line-by-line technique impractical for the window regions and H_2O absorption bands. Therefore, the water vapor transmittances given by Möller and Raschke (1964) which are good for only relatively broad spectral intervals were employed, and the IRIS measurements were integrated over corresponding intervals.

The statistical estimation technique for obtaining humidity profiles has also been applied to selected IRIS spectra. In this approach, the relation

$$\mathbf{r} = \langle \mathbf{r} \rangle + \mathbf{SP}^* (\mathbf{PSP}^* + \mathbf{N})^{-1} \left[\tilde{\mathbf{I}} - \mathbf{I}\left(\langle \mathbf{r} \rangle\right) \right] \tag{14}$$

is employed. Here $\mathbf{r}$ is the vector whose components consist of the estimated relative humidities at various atmospheric levels, S is the covariance matrix for the relative humidity profile

$$S_{ij} = \left\langle \left(r_i - \langle r_i \rangle \right) \left(r_j - \langle r_j \rangle \right) \right\rangle \tag{15}$$

The matrix P is given by

$$P_{ij} = \frac{\partial \mathbf{I}(\nu_i)}{\partial r_j} \tag{16}$$

and N is the instrumental noise covariance matrix. The angular brackets denote ensemble averaging and an asterisk denotes matrix transposition. $\tilde{\mathbf{I}}$ is the vector of measured radiances, and $\mathbf{I}\left(\langle \mathbf{r} \rangle\right)$ is the vector of radiances calculated using the ensemble mean humidity profile. A detailed discussion of equation (14) is given by Conrath (1969).

An example of an application of the statistical estimation technique is shown in Figure 12. A set of selected tropical humidity profiles based on radiosonde data taken at Guam Island was employed in calculating the covariance matrix S and the mean relative humidities $\langle \mathbf{r} \rangle$. To illustrate the usefulness of this method, even in situations which may be considered atypical with reference to the ensemble from which the statistical parameters were derived, Figure 12 shows humidity profiles obtained during a pass of the satellite from south to north across the Inter-Tropical Convergence (ITC). These data were taken off the northern coast of South America during the Barbados Oceanographic and Meteorological Experiment (BOMEX) in July 1969. The dry upper troposphere observed on the north side of the ITC is confirmed by a radiosonde released by a ship in the area. Although the very low humidity is the upper troposphere could not be distinguished from the complete absence of water vapor, the qualitative behavior of the change in the humidity profile in crossing the ITC is well established.

Thus far, only situations have been considered in which the field-of-view of the instrument was essentially cloud-free. However, to obtain truly global coverage, it is necessary to be able to treat the situation in which the instrument field-of-view is partially cloud filled since this will be the case most frequently encountered. The technique considered here for handling the clouds is similar to that suggested by Smith (1969). In this approach, a cloud model is employed which assumes some fraction N of the field-of-view to be filled with clouds represented as a blackbody boundary at pressure level P_c, radiating at the local atmospheric temperature. Thus, it is assumed that the measured radiances can be represented in the form

$$\tilde{I}(\nu) = (1 - N)\, I(\nu) + N\, I_c(\nu, P_c) \tag{17}$$

where $I(\nu)$ is the radiance that would be obtained in the absence of clouds, and $I_c(\nu, P_c)$ is the radiance that would be obtained with a blackbody boundary at level P_c. It is further assumed that the surface temperature is known a priori either from conventional measurements or from determinations made using a high spatial resolution radiometer carried on the satellite. A first estimate of the temperature profile is made using only the more opaque spectral intervals in the range 668 cm^{-1} to 695 cm^{-1} which are not as severely influenced by clouds. This allows estimation of a profile down to about 150 mb, and the interpolation is made between the 150 mb level and the independently specified surface temperature. This first estimate for the temperature profile along with the surface

temperature is then employed in equation (17) to obtain estimates of N and P_c, using measurements in spectral intervals centered at 735 cm^{-1} and 900 cm^{-1}. These cloud parameters are then used to correct the radiances in the interval between 668 cm^{-1} and 710 cm^{-1} to obtain an estimate of the values they would have if the clouds were not present, i.e.,

$$I(\nu) = \tilde{I}(\nu) + \Delta I(\nu, N, P_c) \tag{18}$$

where the correction term is given by

$$\Delta I(\nu, N, P_c) = N\left[I(\nu) - I_c(\nu, N, P_c)\right] \tag{19}$$

The corrected radiances are then used to obtain a new estimate of the temperature profile. This temperature profile is then employed to obtain revised values for N and P_c. The procedure is iterated until N and P_c change by less than specified amounts.

Figures 13 and 14 illustrate the application of the procedure outlined above to IRIS data. The figures show estimates of temperature profiles from two successive spectra taken in the vicinity of Dodge City, Kansas. Both estimates are compared with measurements obtained from a radiosonde released at Dodge City about one half hour later. In Figure 13 the sounding was obtained with an inference of nearly clear conditions; the inference of 4% cloud cover at a very high level could possibly have been due to the presence of thin cirrus. The estimate in Figure 14 from the second spectrum indicated 43% cloud cover at 420 mb.

The overall agreement of the estimate with the radiosonde data is about the same in the two cases. The problem of estimating atmospheric temperatures in the presence of clouds will be considered further in the discussion of atmospheric soundings on a global basis given below.

Unfortunately, an application of this technique to the water vapor estimation does not appear to give satisfactory results in most cases. The reason is that the spectral intervals which contain information on the lower layers containing most of the water vapor, are very sensitive to clouds, requiring large corrections $\Delta I(N, P_c)$ and these corrections cannot be specified with sufficient accuracy at the present time.

VII. ATMOSPHERIC OZONE

Under most conditions, the 1042 cm^{-1} vibration-rotation band of ozone is a conspicuous feature in the IRIS spectra (see Figure 5) and can be utilized to obtain information on ozone. The problem of extracting information on ozone from such spectra has been examined by Prabhakara (1969). In that study a formulation was developed similar to the nonstatistical water vapor estimation technique described above. In the present study the temperature profile needed to compute the ozone distribution is obtained from the 667 cm^{-1} CO_2 band. A representation containing free parameters is assumed for the vertical distribution of ozone, and the free parameters are evaluated by making a least squares fit of the theoretically calculated radiances to the measured radiances in the ozone band, using the Newton-Raphson method.

The vertical ozone distribution was represented in terms of empirical orthogonal functions or characteristic patterns (Obukov, 1960; Holmström, 1963; Mateer, 1965). The empirical orthogonal functions are calculated from ensembles of historical ozone profiles obtained with ozone sondes. They are the eigenvectors of the two level covariance matrix for the vertical ozone distribution. From the resolution and noise equivalent radiance obtained in the IRIS experiment in the region of the 1042 cm^{-1} band, it was found that essentially only one piece of information could be derived on ozone. The single parameter derived was the expansion coefficient of the first empirical orthogonal function. While such a representation provides only relatively crude information on the vertical distribution of ozone, it does, however, permit a meaningful estimate of the total ozone.

Applications of the above technique to IRIS data has been made by Prabhakara, et al. (1970a). In a study involving twenty-five cases for which supporting Dobson spectrometer data existed, they found that the rms error in the total ozone amount, relative to the Dobson measurements, was less than 6%. It was also found that in most cases the effects of clouds on the ozone estimation could be easily eliminated, primarily due to the fact that the bulk of the ozone exists above the atmospheric levels at which clouds occur. For further details on this point and on the empirical deviation of atmospheric transmittances for the 1042 cm^{-1} band, the reader is referred to Prabhakara, et al. (1970a).

Figure 15 (a) shows estimated total ozone in an atmospheric column as a function of latitude, using data from approximately one half of one orbit on

April 22, 1969. The equator crossing for this pass was at 63° West Longitude. In Figure 15 (b), temperatures estimated for the 50 mb level are plotted along with the brightness temperatures derived from the window region. The large spike in the total ozone amount near 40°N is obviously correlated with the minimum in window brightness temperature which in turn is indicative of the presence of high cold clouds. In a case such as this, the background temperature due to the presence of the clouds is very nearly the same as the atmospheric temperature averaged over the ozone distribution so a significant absorption feature no longer exists in the 1042 cm^{-1} region of the spectrum, and the estimate of total ozone becomes inaccurate.

At all other latitudes there appears to be no significant correlation between the ozone amount and the window brightness temperature with the possible exception of the region near 80°S. There appears to be a correlation in the general trends between the 50 mb temperatures and total ozone amount for all latitudes north of 50°S with the exception of the spurious region near 40°N already discussed. However, no obvious correlation exists between 50°S and 80°S. The estimation of ozone on a global scale will be considered further in the following section.

VIII. GLOBAL DISTRIBUTIONS OF TEMPERATURE AND OZONE

Although no effort was made at large scale, real time reduction of IRIS data, global data sets have been generated for selected periods of time to assess the value of the techniques for estimating atmospheric parameters on a global basis.

Figure 16 (a) shows the estimated temperature distribution at the 50 mb level for April 22, 1969, with data taken over a 24 hour period included in the

analysis. It should be emphasized that the temperature obtained for a given level is dependent on the representation chosen for the temperature profile. In this case the representation consisted of fixed anchor points with a linear interpolation as described in Section VI. However, it is found that the estimated temperatures in the Northern Hemisphere are in good general agreement with an analysis based on conventional radiosonde data as shown in Figure 16 (b). Because of the scarcity of conventional data, it was not possible to obtain meaningful comparisons over most of the Southern Hemisphere. In addition to applications to stratospheric studies, the remote sensing of temperature in this portion of the atmosphere is of interest because of its relevance to the supersonic transport.

The global distribution of total ozone obtained from IRIS measurements, also for April 22, 1969, is shown in Figure 17. Again, data taken over a 24 hour period were included in the analysis. Two sets of empirical orthogonal functions were incorporated in the analysis, one from a "low latitude" ensemble for the region between 30°N and 30°S and a "high latitude" ensemble for the regions north of 30°N and south of 30°S. There appears to be some correlation between the 50 mb temperatures and the total ozone in terms of certain large scale features. For example, ozone ridges over the North American continent and over the North Atlantic Ocean correspond to ridges of higher 50 mb temperatures over the same location. Comparisons of the ozone map with the conventional 300 mb Northern Hemisphere chart indicate a general correlation of areas of higher ozone amount with low pressure regions and regions of lower total ozone with

pressure highs; this aspect has been examined in greater detail by Prabhakara, et al. (1970b). It must be emphasized that the smaller scale features in the inferred ozone distribution must be regarded with caution. For example, the ozone spike occurring in Figure 15 (a) is located near the center of the high ozone feature seen in Figure 17 near 40°N, and 75°W, and it is probable that the high clouds in this region are causing some overestimation of the total ozone.

Figure 18 (a) shows temperatures at the 500 mb level obtained from temperature profile estimates from IRIS data in the Northern Hemisphere for July 11, 1969. Surface temperatures employed in the analysis were obtained by spatial and temporal interpolations of the Northern Hemisphere gridded data. The interpolation was necessary to obtain surface temperatures at times and locations coincident with the satellite measurements. A linear, two dimensional spatial interpolation was employed along with a sinusoidal time interpolation having a two hour phase lag with respect to local noon.

In the analysis, spectra were sampled at approximately 5° intervals in latitude along each satellite pass. This resulted in 171 soundings spread over a 24 hour period centered on 1200 GMT. In performing each sounding, a decision was made first on whether or not the instrumental field-of-view contained clouds. This was done by comparing the brightness temperature at 900 cm^{-1} with the surface temperature interpolated from the gridded data. If the brightness temperature was colder than the surface temperature by more than 5°K, it was assumed that the spectral measurements were cloud contaminated, and the sounding was

performed using the two parameter cloud model described in Section VI. Otherwise, the sounding was performed under the assumption that the entire field-of-view was clear. In the sample considered here, 49 cases were judged clear.

An analysis of the 500 mb temperature field based on 1200 GMT radiosonde data is shown in Figure 18 (b). Despite the fact that part of the satellite derived soundings were as much as 12 hours away from the radiosonde data in time, the major features of the two analyses appear to be in general agreement.

For 55 of the soundings, comparisons were made with the closest individual radiosonde. These comparisons indicate a mean error of the 500 mb temperature estimates with respect to the radiosonde values of -1.3°K and an rms error of 2.4°K. These results are admittedly crude, considering the fact that many of the comparisons are poorly correlated in space and time. However, they are indicative of an upper limit on the errors involved.

IX. SURFACE EMISSIVITY EFFECTS

The possiblity of using the characteristics of the spectral emissivity of the surface for remote identification of surface composition is of considerable interest for earth resources applications. For this purpose, it is necessary to use atmospheric "windows" which exist, for example, in the 800 to 1200 cm^{-1} region. Some minerals exhibit the phenomenon of reststrahlen in this spectral interval (Aronson, et al. 1967; Hovis,1966; Hovis, et al. 1968; Hunt and Vincent, 1968; Lyon, 1965). Laboratory measurements show a correlation of the location of

the reststrahlen peaks in the spectral reflectance curves of various silicate bearing minerals with their SiO_2 content. The peak varies from 900 to 1180 cm^{-1} with those samples having the most SiO_2 peaking at higher wave numbers.

To ascertain if the IRIS data show surface emissivity effects, the 800 to 1200 cm^{-1} region of selected spectra are examined. It was necessary to select cases for which the instrumental field-of-view was cloud free and filled by a reasonably homogeneous surface.

Figure 19 shows spectra obtained for two cases of this type on the same orbit. In order to more easily show surface emissivity effects in the window region, the spectra have been plotted in terms of brightness temperature which is defined as the temperature required of a blackbody to produce the observed radiance at a given location in the spectrum.

Spectrum (a) was taken over southern Egypt, while (b) was taken over the Mediterranean Sea. The much warmer surface temperature over the land is responsible for the higher general level of the brightness temperatures in the window region in the spectrum taken over Egypt, compared to that taken over water. The differences observed in the various atmospheric absorption bands can be accounted for by differences in the atmospheric temperature, water vapor, and ozone profiles, as well as the surface temperature differences.

Of significance for the problem of surface emissivity is the relative behavior of the brightness temperatures in the window regions on either side of the 1042 cm^{-1} ozone band. In the spectrum taken over water, the envelopes of brightness

temperature on each side of the ozone band are about the same level. The spectrum taken over Egypt, however, shows a different behavior with the envelope of brightness temperatures on the high wave number side of the ozone band being about 10°K lower than that on the low wave number side. This is consistent with a surface emissivity varying with wave number, having relatively low values on the high wave number side of the ozone band. To explicitly obtain the spectral emissivity of the surface, it would be necessary to remove the atmospheric effects. In general, this is difficult to do with sufficient precision, and a more accurate specification of atmospheric parameters than was available in the case considered here is required. However, it is possible to note the general trend of the emissivity curve which indicates the minimum emissivity occurs at wave numbers smaller than 1100 cm^{-1}, possibly being masked by the ozone band. This would indicate an intermediate SiO_2 content.

This example indicates that, at least under conditions of sufficient homogeneity within the field-of-view, surface spectral emissivity effects can be detected. These effects, while potentially useful for surface studies, can cause problems in the estimation of atmospheric structure. This is due to the fact that the effective brightness temperature for the surface inferred in a window region can lead to erroneous estimates when used in estimating atmospheric temperatures, water vapor or ozone in other spectral regions. However, this problem will probably be restricted to limited geographic locations, such as deserts, and will not be significant over water and vegetated land.

X. SUMMARY

The Nimbus 3 IRIS experiment has demonstrated the feasibility of obtaining high quality infrared spectra from a satellite on a global basis, covering a broad spectral range with a resolution equivalent to 5 cm^{-1}. Both the radiometric precision and accuracy of the measurements are sufficiently good to permit their use in the analysis and testing of atmospheric radiative transfer models and remote sensing techniques.

The comparison of an observed spectrum with a spectrum synthesized, using near simultaneous radiosonde data and line-by-line integration techniques, indicates that the thermal emission spectrum of the earth and atmosphere can be well represented theoretically over large portions of the spectrum between 400 and 1500 cm^{-1}. In addition to the numerous spectral features due to CO_2, H_2O, and O_3, the 1306 cm^{-1} band of CH_4 has been observed, but no features due to other minor atmospheric constituents have yet been positively identified. A limiting factor in comparisons of this type is the need to specify with a high degree of precision the atmospheric temperatures and the vertical distributions of optically active gases within the field-of-view at the time the spectrum is taken. It is necessary to have in situ measurements which are nearly simultaneous in space and time in a region which is homogeneous over an area the size of the instrumental field-of-view. Such conditions are difficult to obtain, particularly with respect to water vapor, which is highly variable spatially and temporally.

The usefulness of the data from the IRIS experiment for obtaining remote soundings of atmospheric temperature, water vapor, and ozone was demonstrated

by applications of radiometric inversion techniques to selected data samples. A nonstatistical technique was employed for estimating temperature profiles along with both statistical and nonstatistical methods for obtaining humidity profiles. Comparisons with individual radiosondes indicate useful temperature profiles can be obtained under both clear and cloudy conditions. The most severe limitation of the temperature estimation technique is the necessity for an independent specification of the surface temperature in order to obtain results under cloudy conditions. The techniques employed here were found to give good water vapor estimates in the lower troposphere only under essentially cloud free conditions.

It has been found that while measurements in the 1042 cm^{-1} band yields only crude information on the vertical distribution of ozone, the inferred total ozone in an atmospheric column is in good agreement with Dobson spectrophotometer measurements. The influence of clouds on the total ozone determination appears to be slight except under special circumstances when the cloud temperature is nearly the same as the atmospheric temperature averaged over the ozone distribution. The ozone, as well as the water vapor determination, also becomes inaccurate when the atmosphere is nearly isothermal as sometimes occurs in the winter polar regions.

While no operational application was intended for IRIS data, temperature profiles and total ozone amounts have been obtained on a global basis for selected days. An analysis of temperatures for 500 mb in the Northern Hemisphere, based on IRIS data, compares favorably with a similar analysis using conventional

radiosondes within the limits imposed by the time smearing of the satellite data. The total ozone amount could not be compared directly with conventional ozone data because of the sparce coverage of the latter. However, comparison with a conventional 300 mb height map indicates correlations with pressure height features.

The space and time distribution of the obtained temperature and humidity profiles should make this body of data useful for tests of numerical circulation models as well as for the planning of future programs of atmospheric research, such as GARP, for example.

Examination of spectra from selected geographic locations has revealed surface emissivity effects in the atmospheric window region. Spectra taken over southern Egypt show that the brightness temperature on the high wave number side of the 1042 cm^{-1} O_3 band decreases by as much as 10°K relative to the brightness temperature on the low wave number side. While it is not possible to remove the atmospheric effects and derive the surface emissivity explicity, in the example considered, it is possible to infer the qualitative behavior of the dependence of emissivity on wave number. While the observed emissivity effects may be of value for surface studies, they can cause problems in remote atmospheric sounding over land areas devoid of vegetation, such as deserts.

The analyses of IRIS Nimbus 3 data presented here are by no means exhaustive. However, they do represent an attempt to apply these data to some of the fundamental problems of remote sensing and to illustrate potential uses of data of this type.

XI. ACKNOWLEDGMENTS

The authors are indebted to the many members of the Nimbus Project whose efforts contributed to the success of the interferometer experiment. The computer programming assistance of G. N. Wolford and H. W. Powell is gratefully acknowledged. The analyses necessary for constructing the temperature and ozone maps were performed by Joseph Steranka.

XII. REFERENCES

1. Anding, D., Band-model methods for computing atmospheric slant-path molecular absorption, IRIA State-of-the-art Report, Willow Run Laboratories, Univ. of Michigan, 1967.

2. Aronson, J. R., A. G. Emslie, R. V. Allen and H. G. McLinden, Studies of the middle and far infrared spectra of mineral surfaces for application in remote compositional mapping of the moon and planets, J. Geophys. Res., 72, 687, 1967.

3. Benedict, W. S., and R. F. Calfee, Line parameters for the 1.9 and 6.3 micron water vapor bands, ESSA Professional Paper 2, Environmental Science Services Administration, June 1967.

4. Benedict, W. S., and L. D. Kaplan, private communication of unpublished values, 1967.

5. Bignell, K., F. Saiedy and P. A. Sheppard, On the atmospheric infrared continuum, J. Opt. Soc. Am., 53, 466, 1963.

6. Bolle, H. -J., Investigation of the infrared emission spectrum of the atmosphere and earth, Final Report, Ludwig-Maximilians-Universität, Meteorologisches Institut, München, Germany, July 31, 1965.

7. Bolle, H. -J., Infrarotspektroskopie als hilfsmittel und gegenstand meteorologischer and planetarischer forschung, Meteorologisches Institut, der Ludwig-Maximilians-Universität, München, Germany, Juli 1967.

8. Burch, D. E., Absorption of infrared radiant energy by CO_2 and H_2O. III. Absorption by H_2O between 0.5 and 36 cm^{-1} (278μ - 2 cm), J. Opt. Soc. Am., 58, 1383, 1968.

9. Burch, D. E., Investigation of the absorption of infrared radiation by atmospheric gases, Aeronutronic Report U-4784, Philco-Ford Corp. Aeronutronic Division, January 31, 1970.

10. Burch, D. E., D. A. Gryvnak, R. R. Patty, and C. E. Bartky, Absorption of infrared radiant energy by CO_2 and H_2O. IV. Shapes of collison-broadened CO_2 lines, J. Opt. Soc. Am. 59, 267, 1969.

11. Burroughs, W. J., R. G. Jones, and H. A. Gebbie, A study of submillimetre atmospheric absorption using the HCN maser, J. Quant. Spectrosc. Radiat. Transfer, 9, 809, 1969b.

12. Chahine, M. T., Determination of the temperature profile in an atmosphere from its outgoing radiance, J. Opt. Soc. Am., 58, 1634, 1968.

13. Clough, S. A., Private communication, 1970.

14. Clough, S. A., and F. X. Kneizys, Ozone absorption in the 9.0 micron region, Air Force Cambridge Research Laboratories Report No. AFCRL-65-862, November 1965.

15. Conrath, B. J., Inverse problems in radiative transfer: a review, Proceedings of the XVIIIth International Astronautical Congress, edited by M. Lunc, 339, 1968.

16. Conrath, B. J., On the estimation of relative humidity profiles from medium-resolution infrared spectra obtained from a satellite, J. Geophys. Res. 74, 3347, 1969.

17. Drayson, S. R., and C. Young, The frequencies and intensities of carbon dioxide absorption lines between 12 and 18 microns, Univ. of Michigan Report No. 08183-1-1, High Altitude Engineering Laboratory, November 1967.

18. Farmer, C. B., Extinction coefficients and computed spectra for the rotational band of water vapour between 0.7 and 1000 cm^{-1}, E. M. I. Ltd., Hayes, Middlesex, England, Report No. DMP 2780, April, 1967.

19. Gray, L. D., Calculations of carbon dioxide transmission Part I—the 9.4μ and 10.4μ bands, J. Quant. Spectrosc. Radiat. Transfer, 7, 143, 1967.

20. Green, A. E. S., and M. Griggs, Infrared transmission through the atmosphere, Appl. Opt., 2, 561, 1963.

21. Hanel, R., and B. Conrath, Interferometer experiment on Nimbus 3: preliminary results, Science, 165, 1258, September 19, 1969.

22. Hanel, R. A., B. Schlachman, F. D. Clark, C. H. Prokesh, J. B. Taylor, W. M. Wilson, and L. Chaney, The Nimbus 3 Michelson interferometer, to be published in Appl. Opt., June 1970.

23. Harries, J. E., W. J. Burroughs, and H. A. Gebbie, Millimetre Wavelength spectroscopic observations of the water dimer in the vapour phase, J. Quant. Spectrosc. Radiat. Transfer, 9, 799, 1969.

24. Holström, I., On a method for parametric representation of the state of the atmosphere, Tellus, 15, 127, 1963.

25. Hovis, W. A., Optimum wavelength intervals for surface temperature radiometry, Appl. Opt. 5, 815, 1966.

26. Hovis, W. A., L. R. Blaine, and W. R. Callahan, Infrared aircraft spectra over desert terrain 8.5μ to 16μ, Appl. Opt., 1, 1137, 1968.

27. Hunt, G. R., and R. K. Vincent, The behavior of spectral features in the infrared emission from particulate surfaces of various grain sizes, J. Geophys. Res., 73, 6039, 1968.

28. Kaplan, L. D., Inference of atmospheric structure from remote radiation measurements, J. Opt. Soc. Am., 49, 1004, 1959.

29. King, J. I. F., The radiative heattransfer of planet earth, Scientific Uses of Earth Satellites, Second Edition, edited by J. A. Van Allen, Univ. of Mich. Press, 316 pp., 1958.

30. King, J. I. F., Inversion by slabs of varying thickness, J. Atmos. Sc., 21, 324, 1964.

31. Kunde, V. G., Theoretical molecular line absorption of CO in late-type atmospheres, Ap. J., 153, 435, 1968.

32. Kunde, V. G., Opacity-probability distribution functions for carbon monoxide at elevated temperatures, Ap. J., 158, 1167, 1969.

33. Kyle, T. G., Line parameters of the infrared methane bands, Scientific Report No. 1, Air Force Cambridge Research Laboratories, ARCRL-68-0521, October 1968.

34. Lyon, R. J. P., Analysis of rocks by spectral infrared emission (8 - 25μ), Econ. Geol., 60, 715, 1965.

35. Mateer, C. L., On the information content of umkehr observations, J. Atmos. Sc., 22, 370, 1965.

36. Migeotte, M., L. Neven, and J. Swensson, The solar spectrum from 2.8 to 23.7 microns: Part I. Photometric atlas, Part II. Measures and identifications, Institute D'Astrophysique de l'Universite de Liege, 1957.

37. Möller, F., and E. Raschke, Evaluation of Tiros 3 radiation data, NASA Contractor Report CR-112, 1964.

38. Möller, F., and E. Raschke, Problems of meteorological observations from satellites, Sp. Sci. Rev., 9, 90, 1969.

39. Nimbus 3 User's Guide, The Nimbus Project, Goddard Space Flight Center, March 1970.

40. Obukohov, A. M., The statistically orthogonal expansion of emperical functions, Izvestiya, Seriya Geoficizicheskaya, Akad. Nauk SSSR, No. 3, 432, 1960.

50. Strand, O. N., and E. R. Westwater, Minimum rms estimation of the numerical solution of a Fredholm integral equation of the first kind, SIAM J. Numerical Analysis, 5, 287, 1968.

51. Varanasi, P., S. Chou, and S. S. Penner, Absorption coefficients for water vapor in the 600-1000 cm^{-1} region, J. Quant. Spectrosc. Radiat. Transfer, 8, 1537, 1968.

52. Viktorova, A. A., and S. A. Zhevakin, Absorption of microwaves in air by water-vapor dimers, Soviet Physics-Doklady, 11, 1065, June 1967.

53. Wark, D. Q., On indirect soundings of the stratosphere from satellites, J. Geophys. Res., 66, 77, 1961.

54. Wark, D. Q., and H. E. Fleming, Indirect measurements of atmospheric temperature profiles from satellites, 1, Introduction, Mon. Wea. Rev., 94, 351, 1966.

55. Wark, D. Q. and D. T. Hilleary, Atmospheric temperature: successful test of remote probing, Science, 165, 1256, 1969.

41. Penner, S. S., and P. Varanasi, Spectral absorption coefficients in the pure rotation spectrum of water vapor, J. Quant. Spectrosc. Radiat. Transfer, 1, 687, 1967.

42. Plyler, E. K., and E. F. Barker, The infrared spectrum and the molecular configuration of N_2O, Phy. Rev., 38, 1827, 1931 .

43. Prabkahara, C., Feasibility of determining atmospheric ozone from outgoing infrared energy, Mon. Wea. Rev., 97, 307, 1969.

44. Prabhakara, C., B. J. Conrath, R. Hanel, and E. J. Williamson, Remote sensing of atmospheric ozone using the 9.6μ band, to be published in J. Atmos. Sc., July 1970a.

45. Prabhakara, C., B. J. Conrath, L. J. Allison, and J. Sterenka, Seasonal and geographic variations of atmospheric ozone derived from Nimbus 3, in preparation, 1970b.

46. Rodgers, C. D., Satellite infrared radiometer; a discussion of inversion methods, Univ. of Oxford Clarendon Lab. Mem. 66.13, 25 pp., 1966.

47. Saiedy, F., Thesis, London Univ., 1960.

48. Saiedy, F., and D. T. Hilleary, Remote sensing of surface and cloud temperatures using the 899-cm interval, Appl. Opt., 6, 911, 1967.

49. Smith, W. L., Statistical estimation of the atmosphere's geopotential height distribution from satellite radiation measurements, ESSA Technical Report NESC 48, 1969.

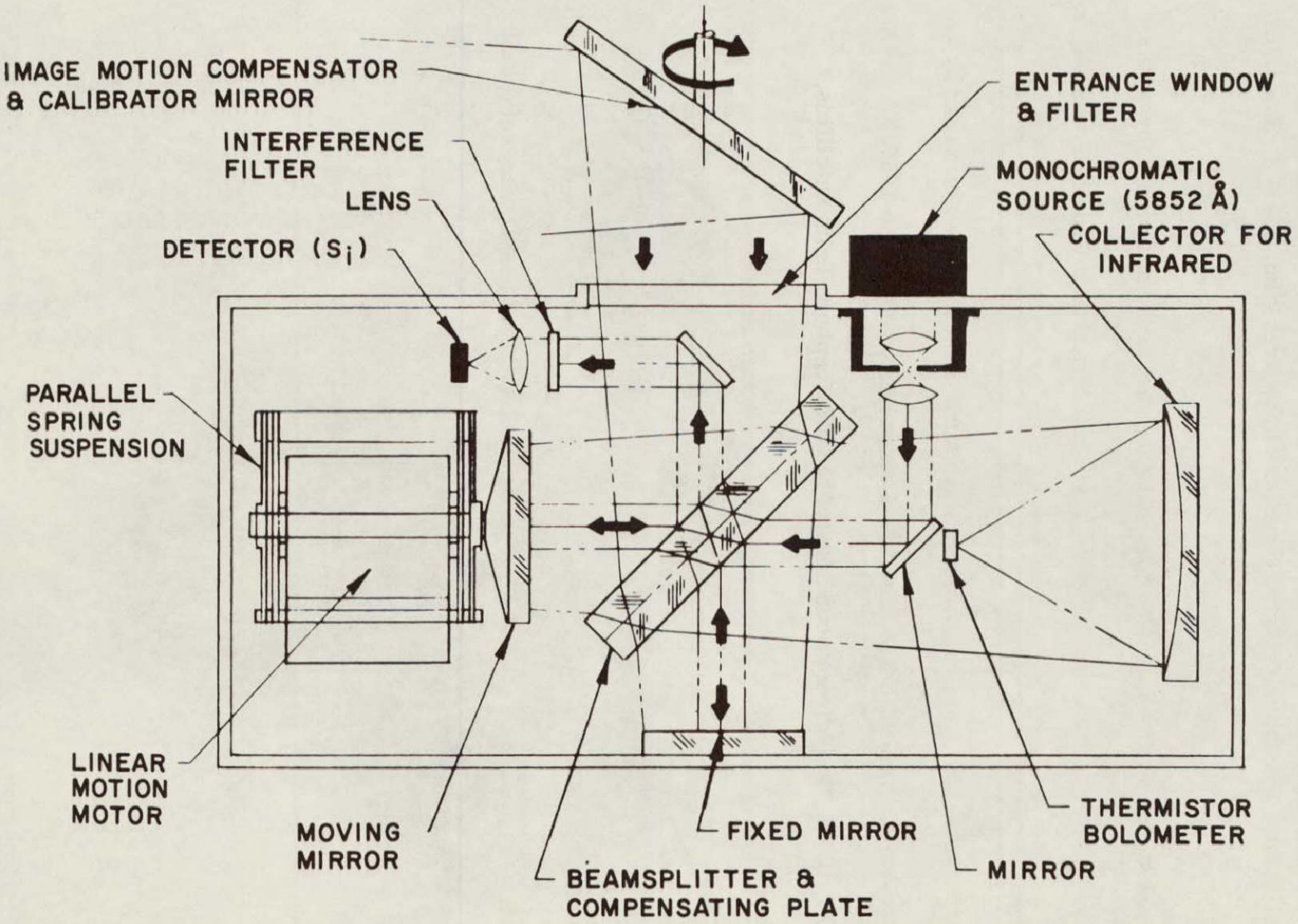

Figure 1. Schematic cross section of the infrared interferometric spectrometer (IRIS). Coaxial with the infrared interferometer is the fringe control interferometer which provides the wave number standard and the signal for the phase locked loop operation of the Michelson mirror. The physical displacement of this mirror is 0.2 cm.

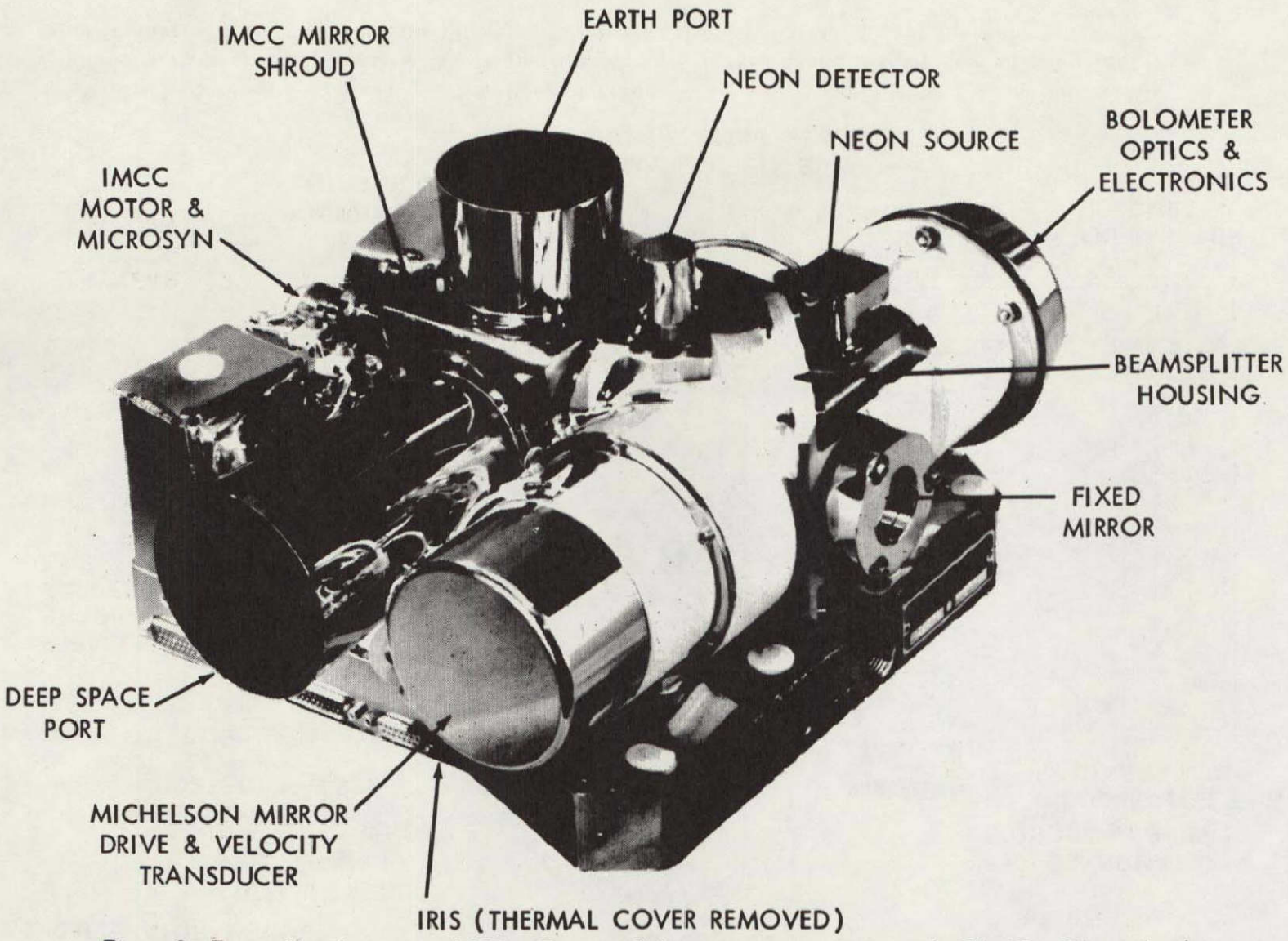

Figure 2. External configuration of IRIS. The overall dimensions are approximately 20 × 23 × 30 cm. Another smaller module containing the power supply and other electronic circuits are not shown.

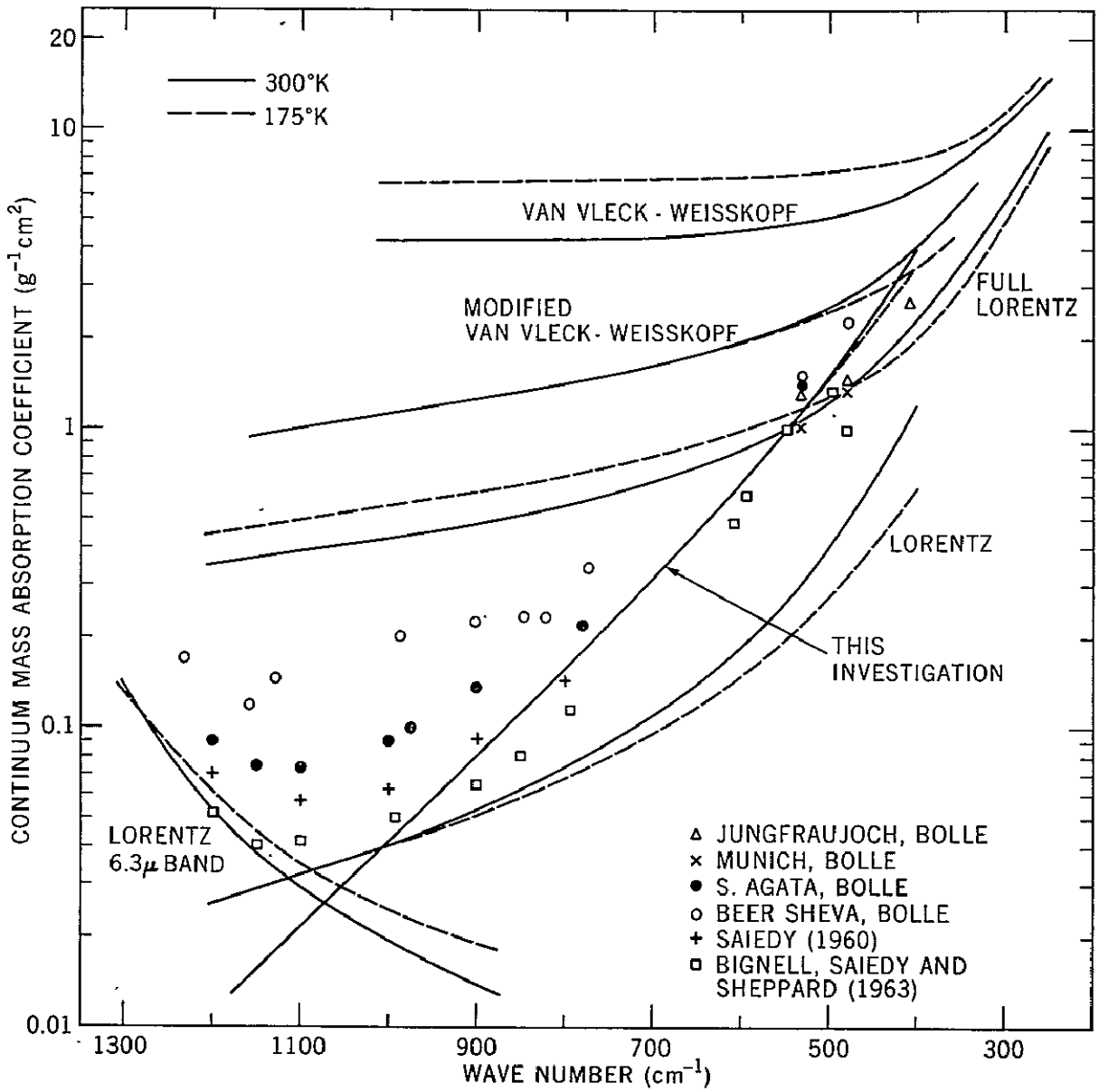

Figure 4. The continuum mass absorption coefficient is shown for several types of theoretical pressure-broadened H_2O line shapes for the atmospheric "windows" in the 500 and 1000 cm^{-1} region. Continuum absorption coefficients derived from atmospheric emission measurements are also shown. The scatter in the observed coefficients reflects differences in aerosols and in the effect of H_2O self-broadening. The values adopted in this investigation are noted.

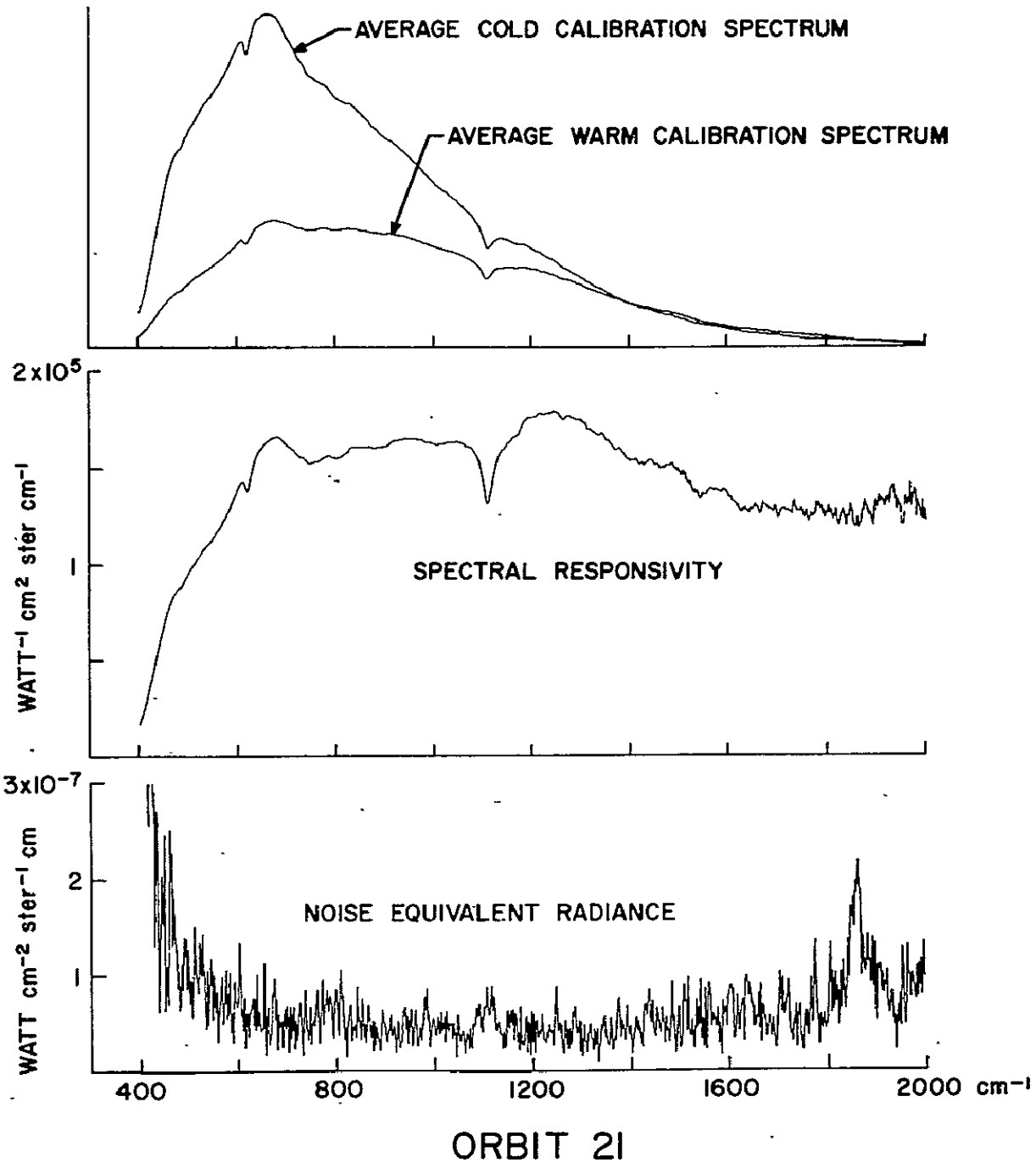

Figure 3. The orbital averages of cold and warm blackbody spectra and the spectral responsivity calculated from the calibration spectra. The ordinate for the calibration spectra is in arbitrary units.

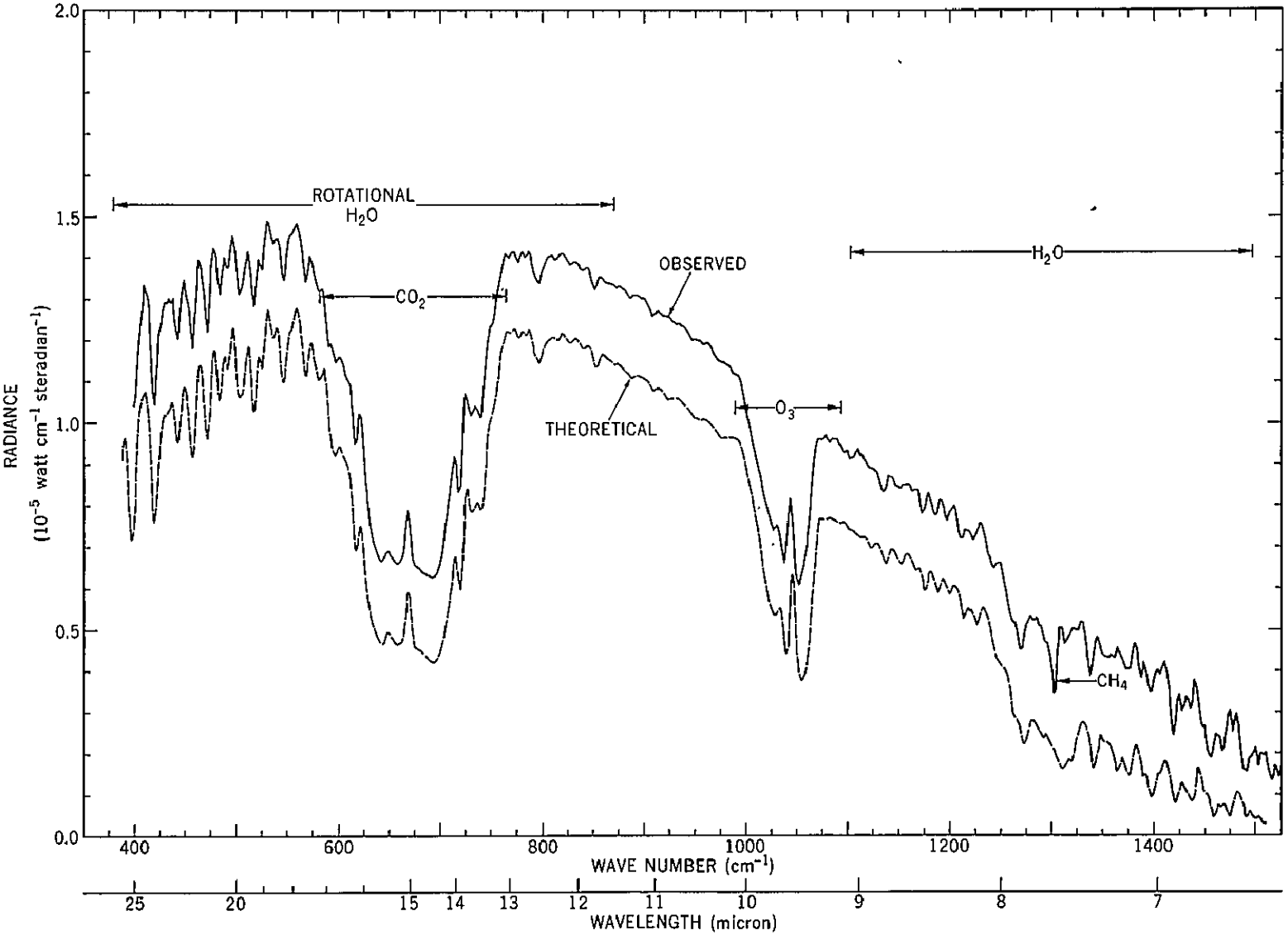

Figure 5. Comparison of the observed and theoretical radiances for a clear atmosphere over the Gulf of Mexico at 1734 GMT, April 22, 1969. The observed spectrum is displaced upward 0.2×10^{-5} watt cm^{-1} ster^{-1} for clarity.

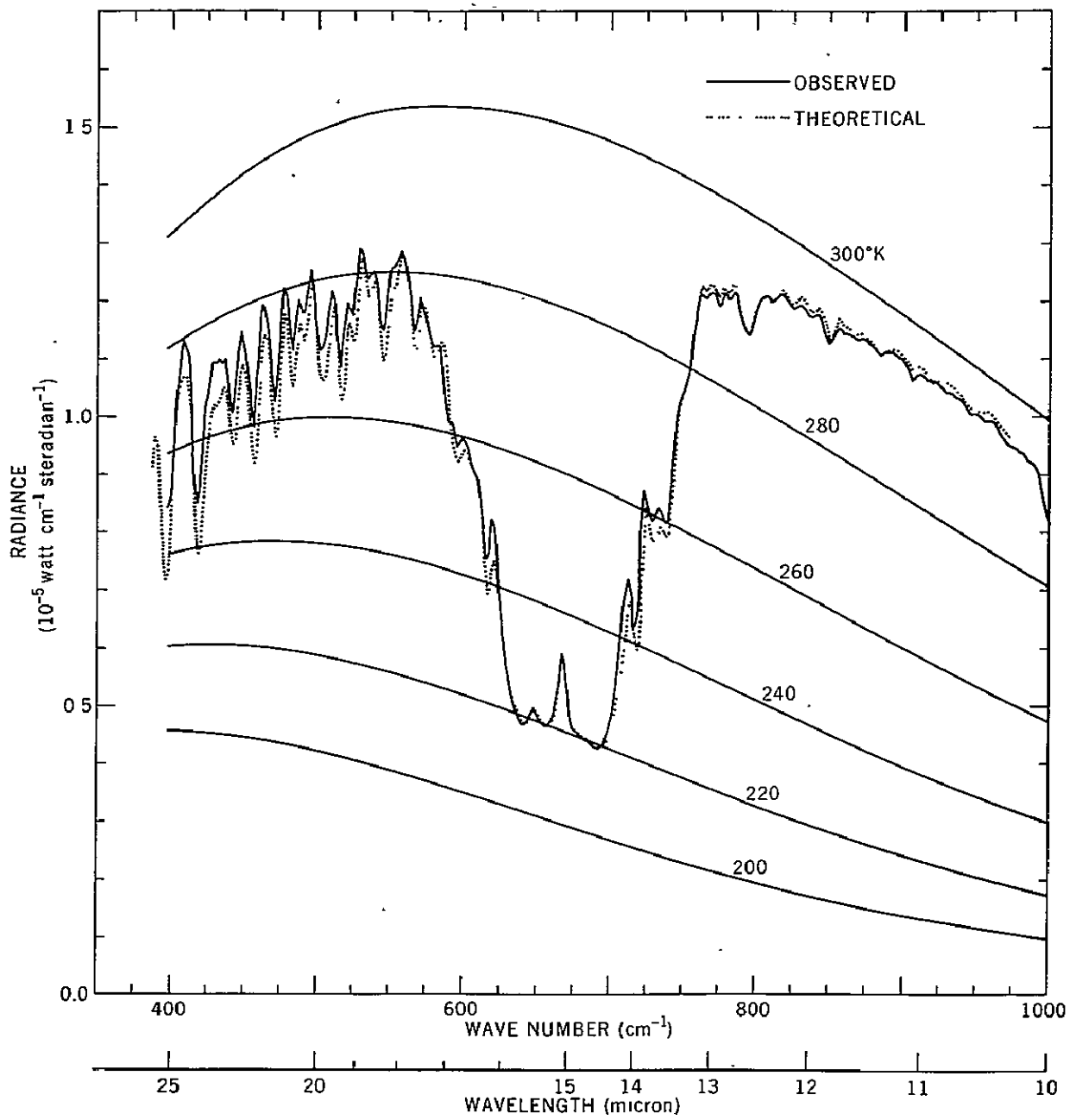

Figure 6. The 400-1000 cm^{-1} portion of the spectrum shown in Figure 5 is presented on an enlarged scale with no ordinate displacement.

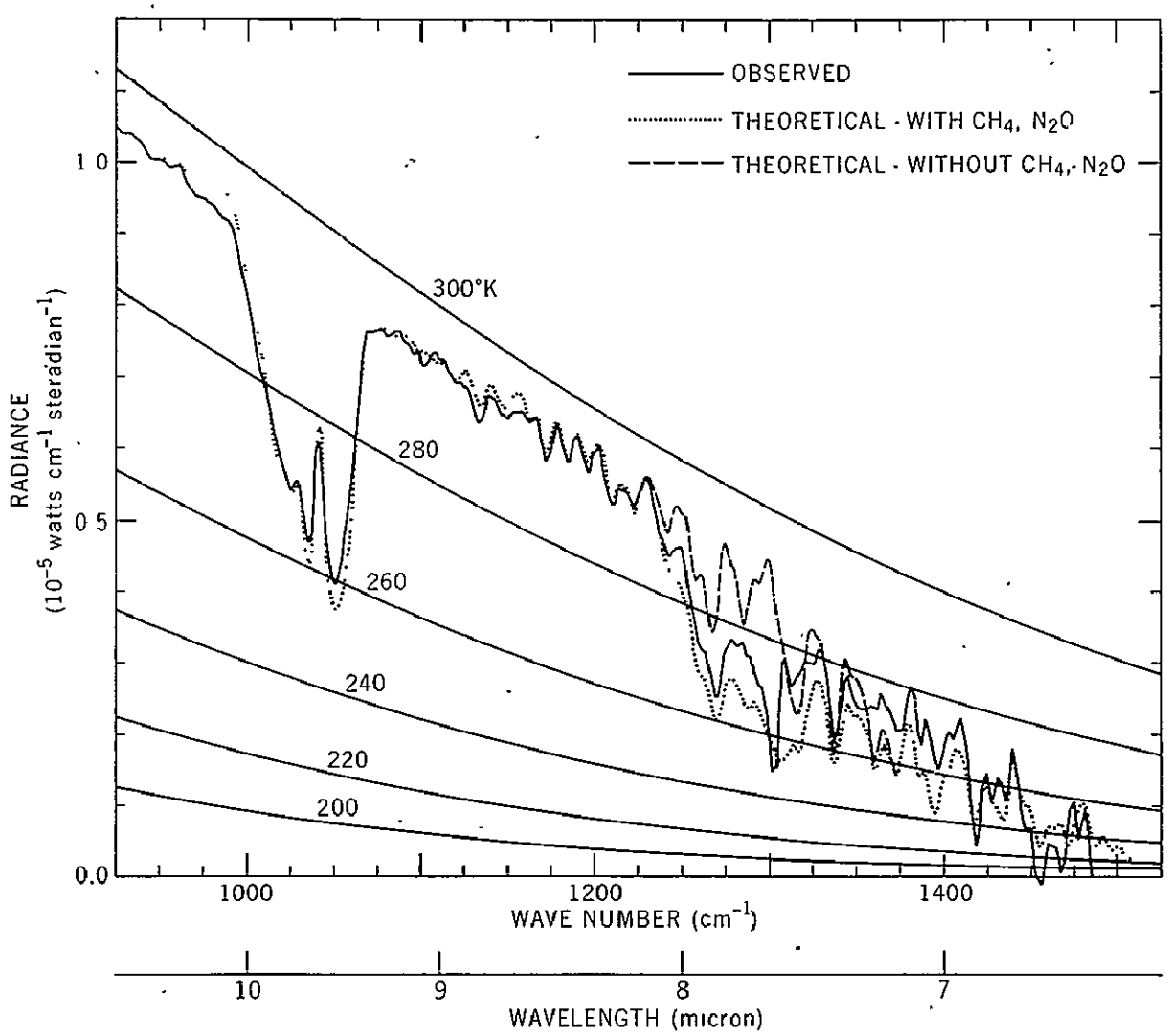

Figure 7. The 1000-1450 cm^{-1} portion of the spectrum shown in Figure 5 is presented on an enlarged scale with no ordinate displacement. The effect of molecular absorption by CH_4 and N_2O is also illustrated.

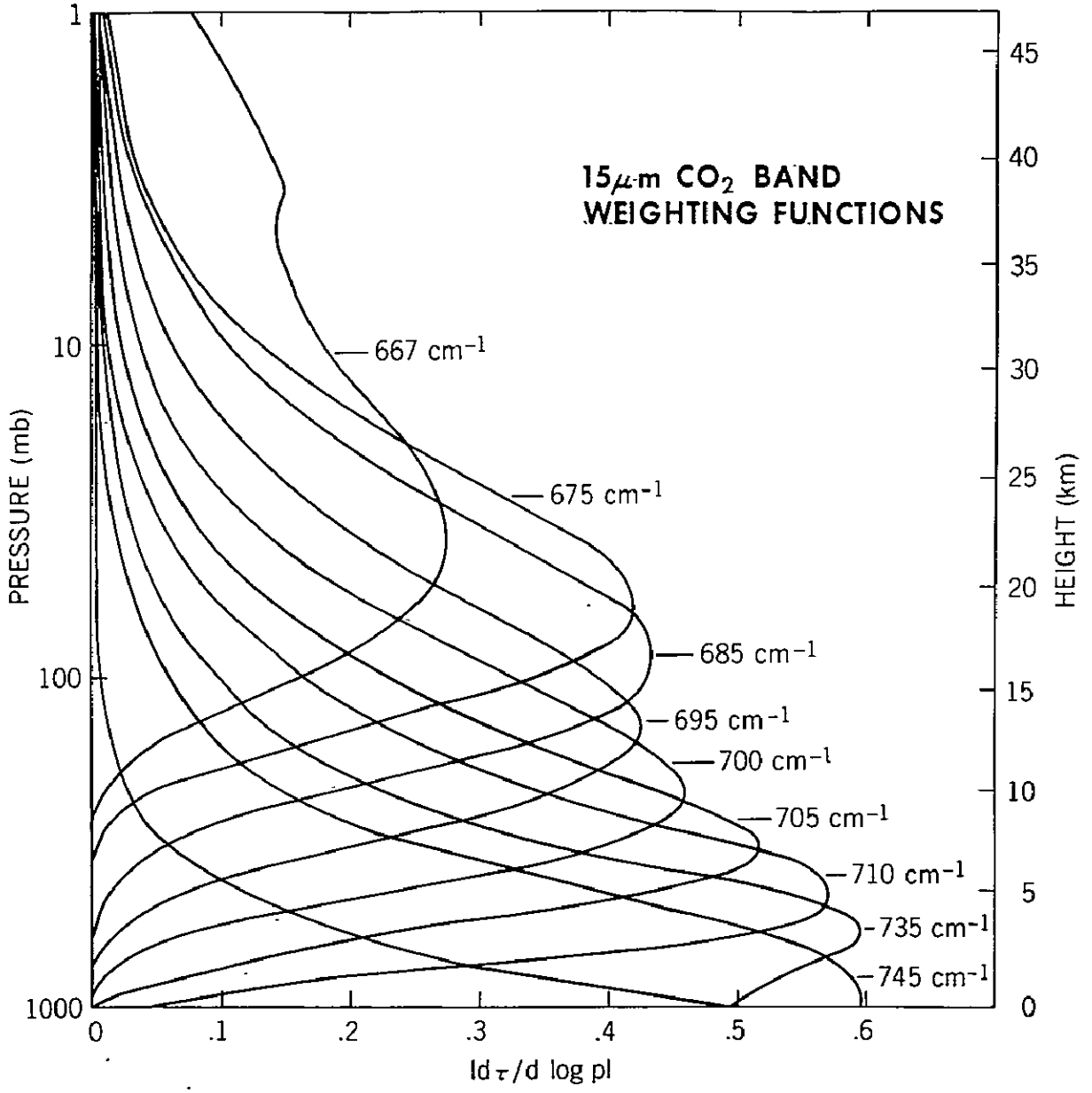

Figure 8. Atmospheric weighting functions for the 667 cm^{-1} (15 μ m) CO_2 absorption band. The curves were calculated assuming an instrument function 5 cm^{-1} wide at the half maximim point, centered on the wavenumbers indicated.

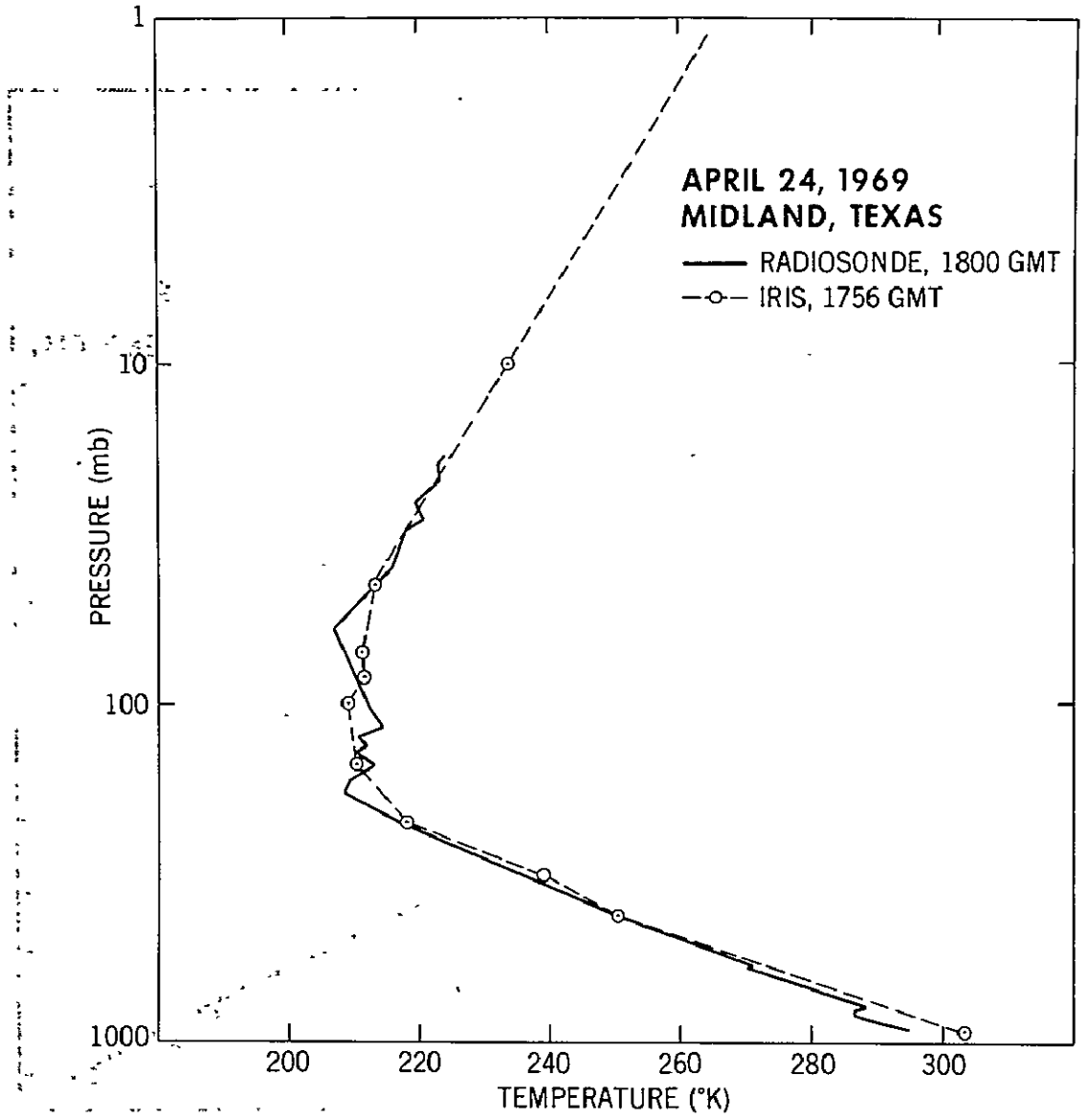

Figure 10a. Temperature profile.

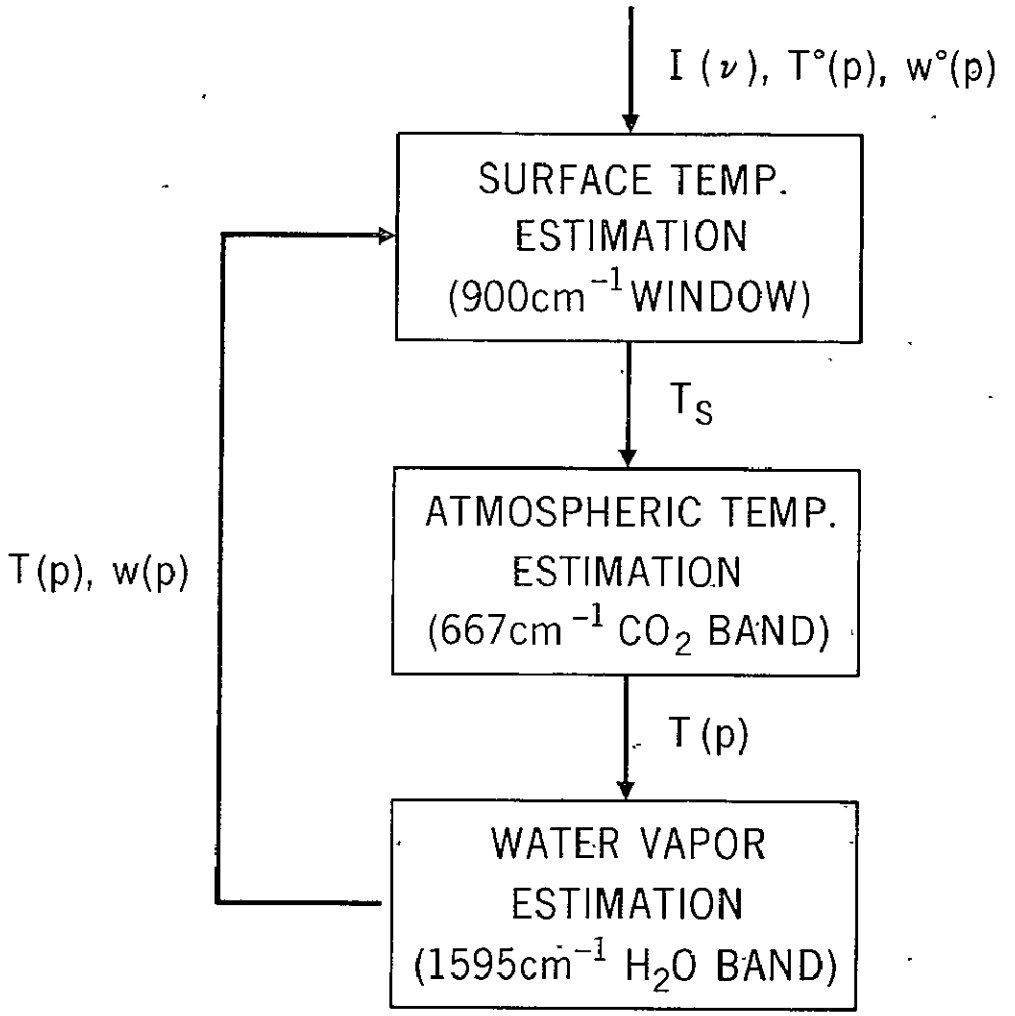

Figure 9. Schematic diagram illustrating the computational approach followed in obtaining temperature and humidity profiles. Initial guesses for temperature $T^{\circ}(p)$ and water vapor mixing ratio $w^{\circ}(p)$ are employed.

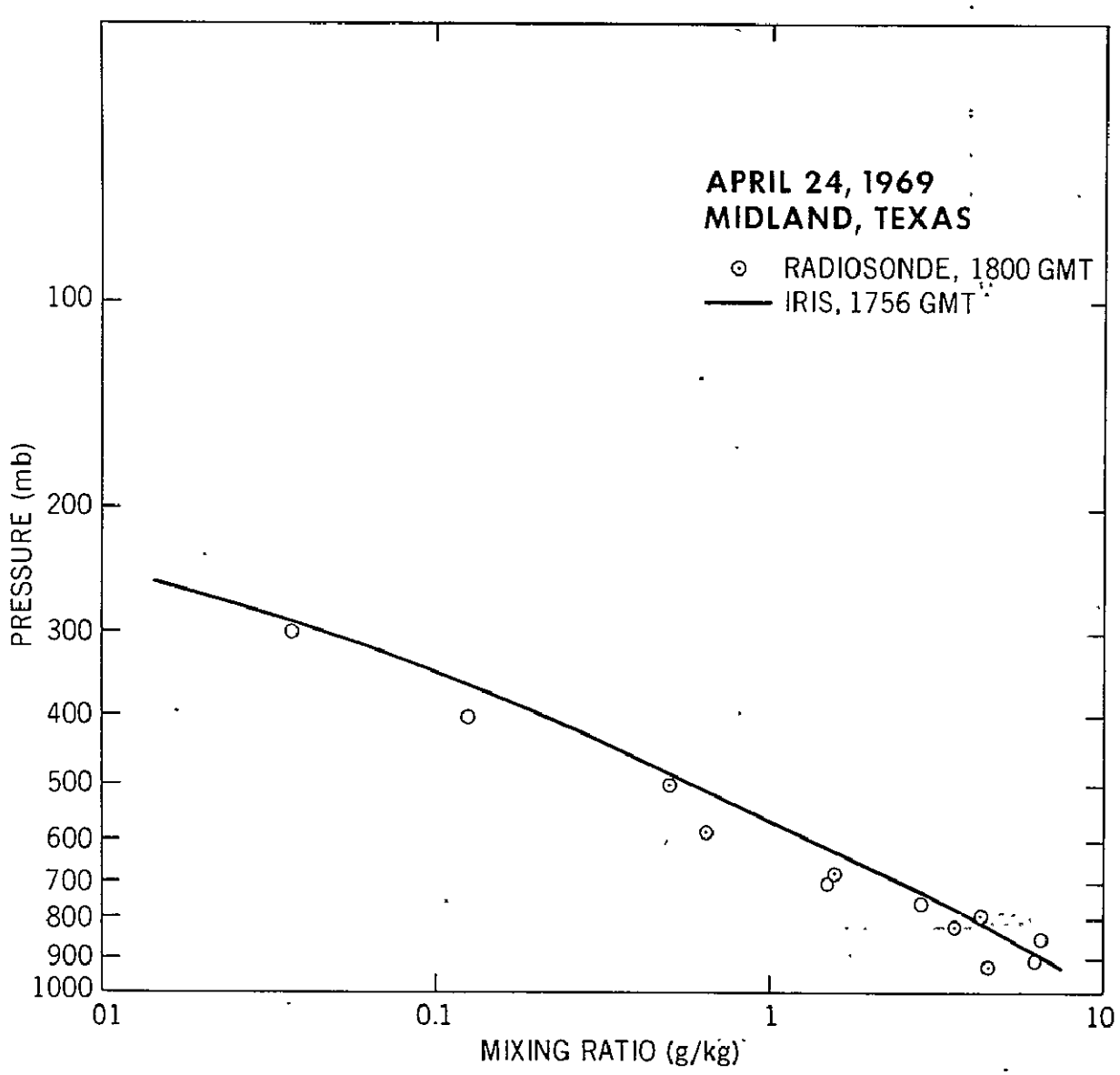

Figure 10b. Water vapor mixing ratio profile obtained from the satellite measurements and compared with measurements obtained from a near simultaneous radiosonde flight. A mid-latitude example is shown here.

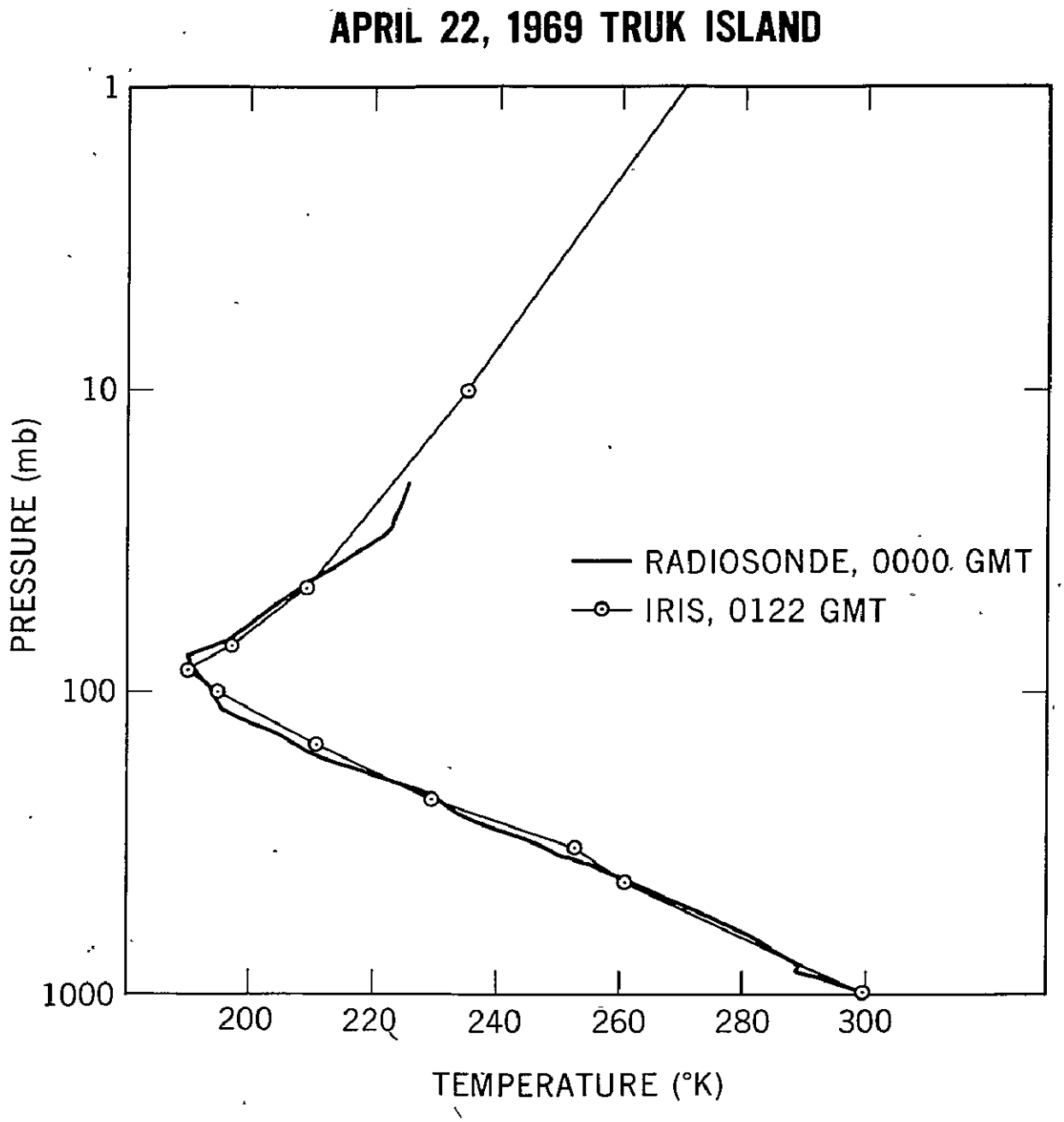

Figure 11a. A Temperature profile.

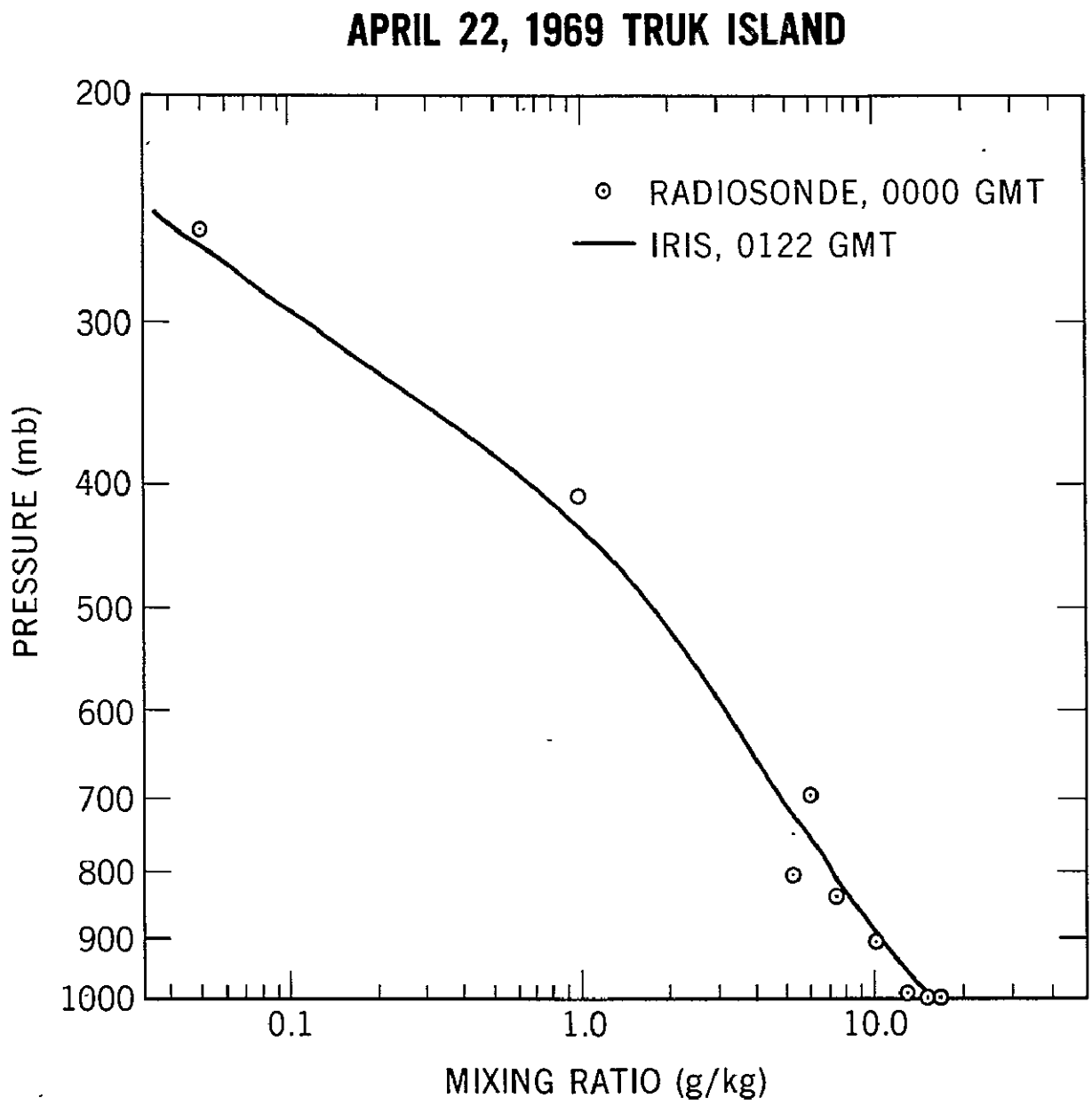

Figure 11b: Water vapor mixing ratio profile obtained from the satellite measurements and compared with measurements obtained from a near simultaneous radiosonde flight. A low-latitude example is shown here.

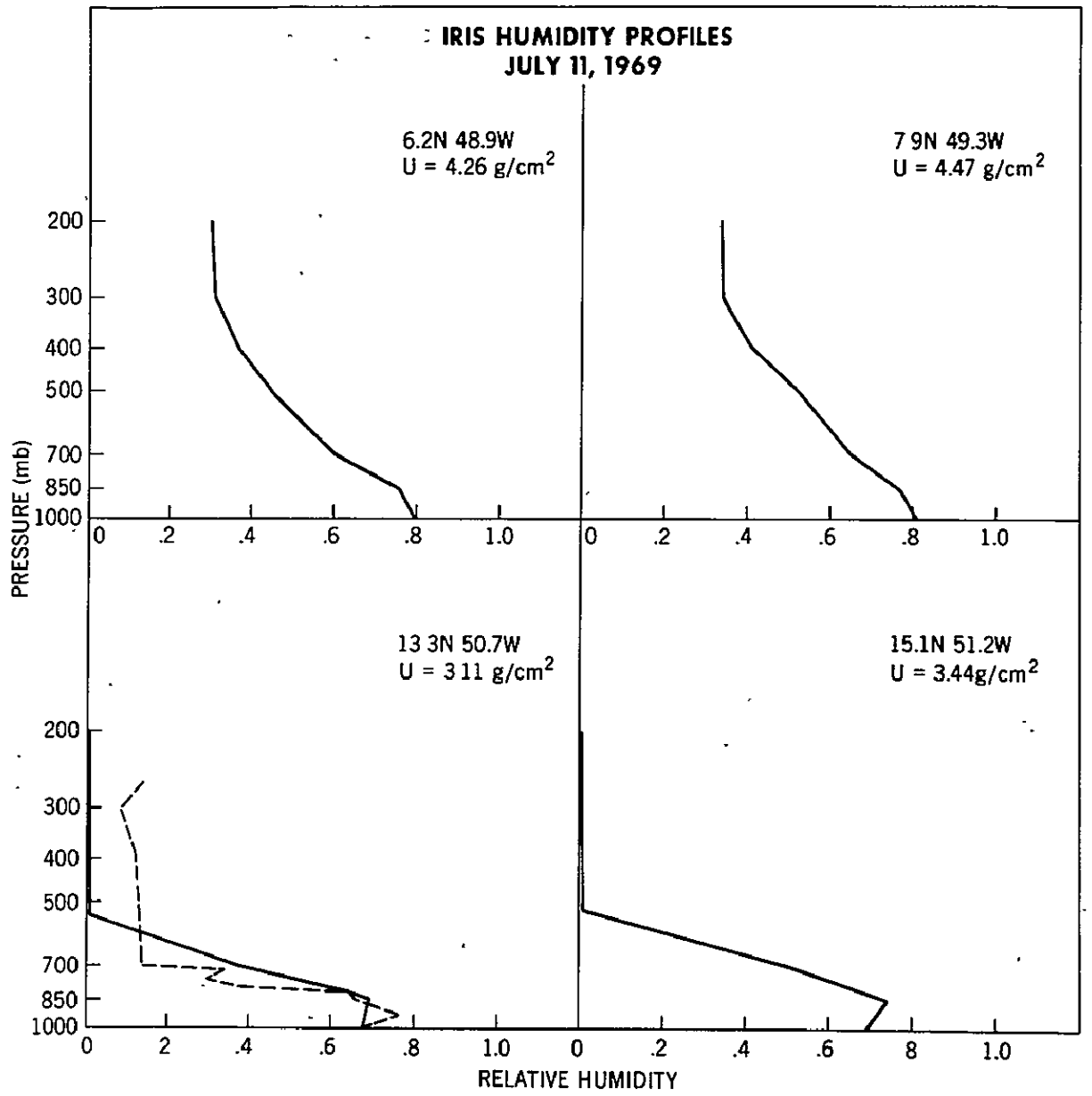

Figure 12. Relative humidity profiles obtained using a statistical estimation technique. The profiles were derived from data obtained during a passage of the satellite across the Inter-Tropical Convergence (ITC) on July 11, 1969 in the area of the Barbados Oceanographic and Meteorological Experiment (BOMEX). The integrated water content in an atmospheric column u is indicated in each case. Comparison of the profile at 13.3°N 50.7°W with radiosonde data (broken line) obtained from a ship in the area indicates that the dry upper air north of the ITC has been detected even though it is anomolous relative to the ensemble employed in the statistical estimation.

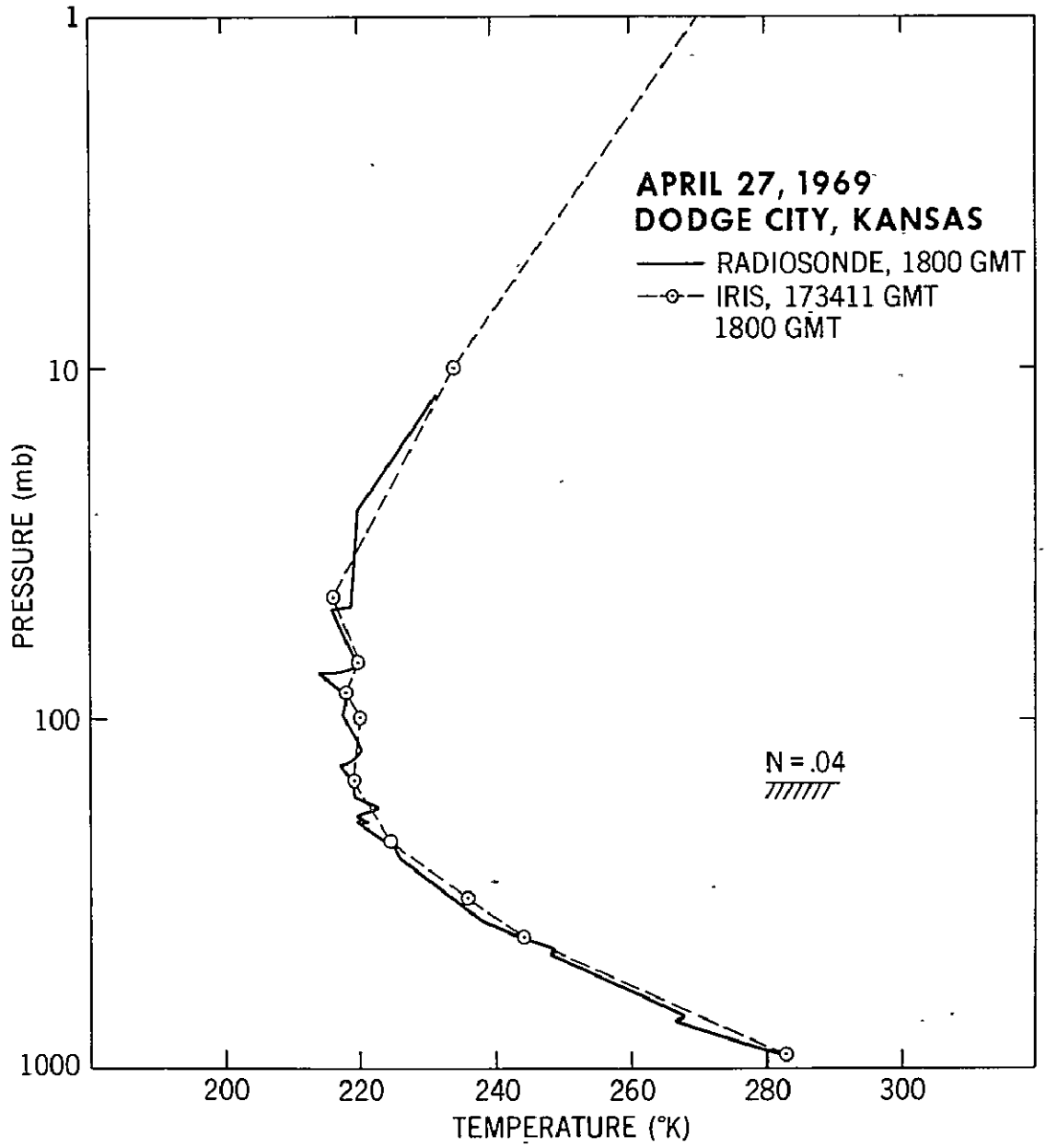

Figure 13. Estimate of a temperature profile compared with a nearby radiosonde. A computational scheme designed for a partly cloud filled instrumental field-of-view was employed. A 4% cloud cover at 150 mb was inferred, which is essentially equivalent to the absence of clouds with this estimation technique.

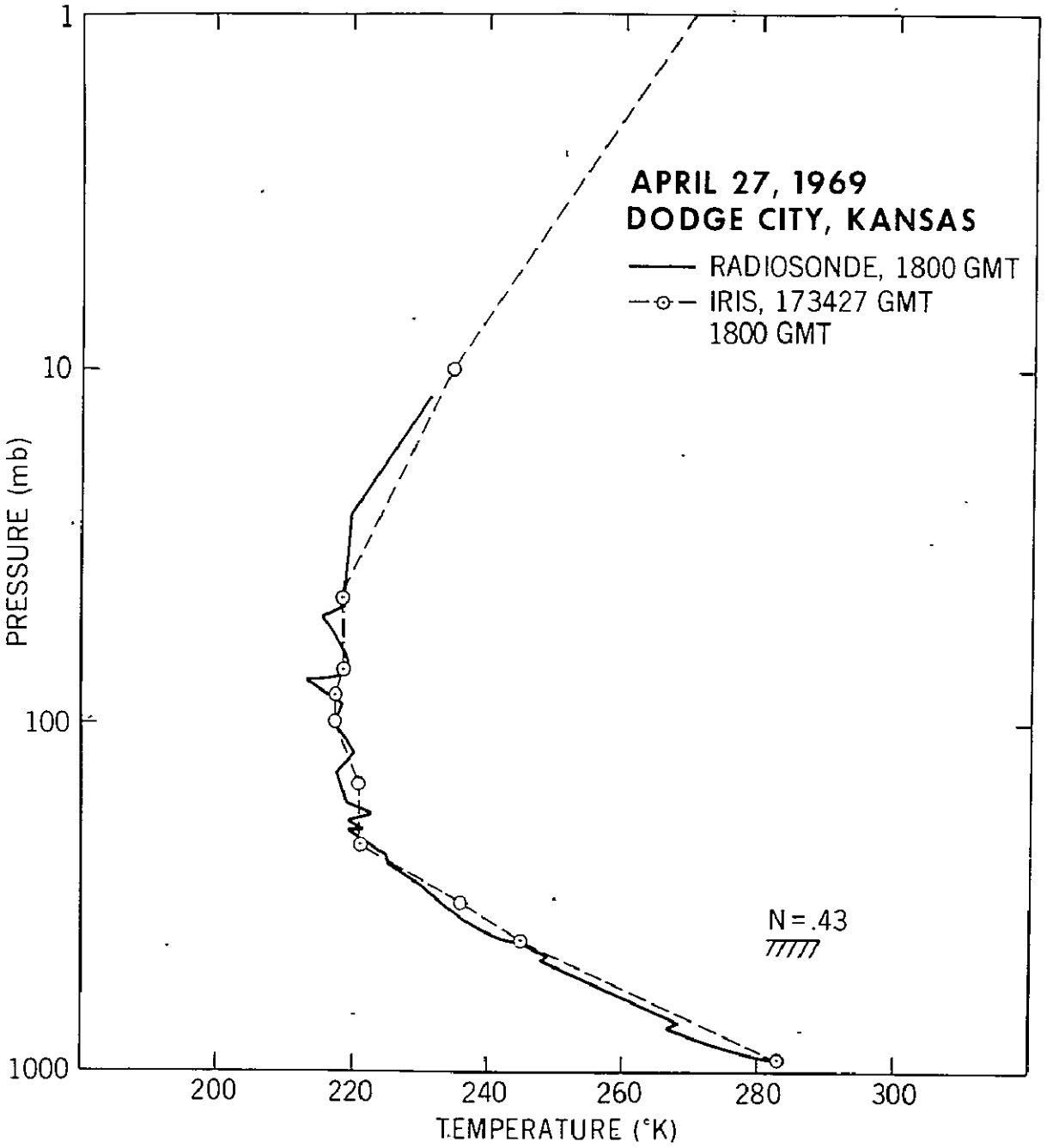

Figure 14. Estimation of a temperature profile obtained from data acquired 16 seconds after that of Figure 13. The cloud cover was inferred to be 43% at 420 mb. A comparison is made with the same radiosonde data as that employed in Figure 13.

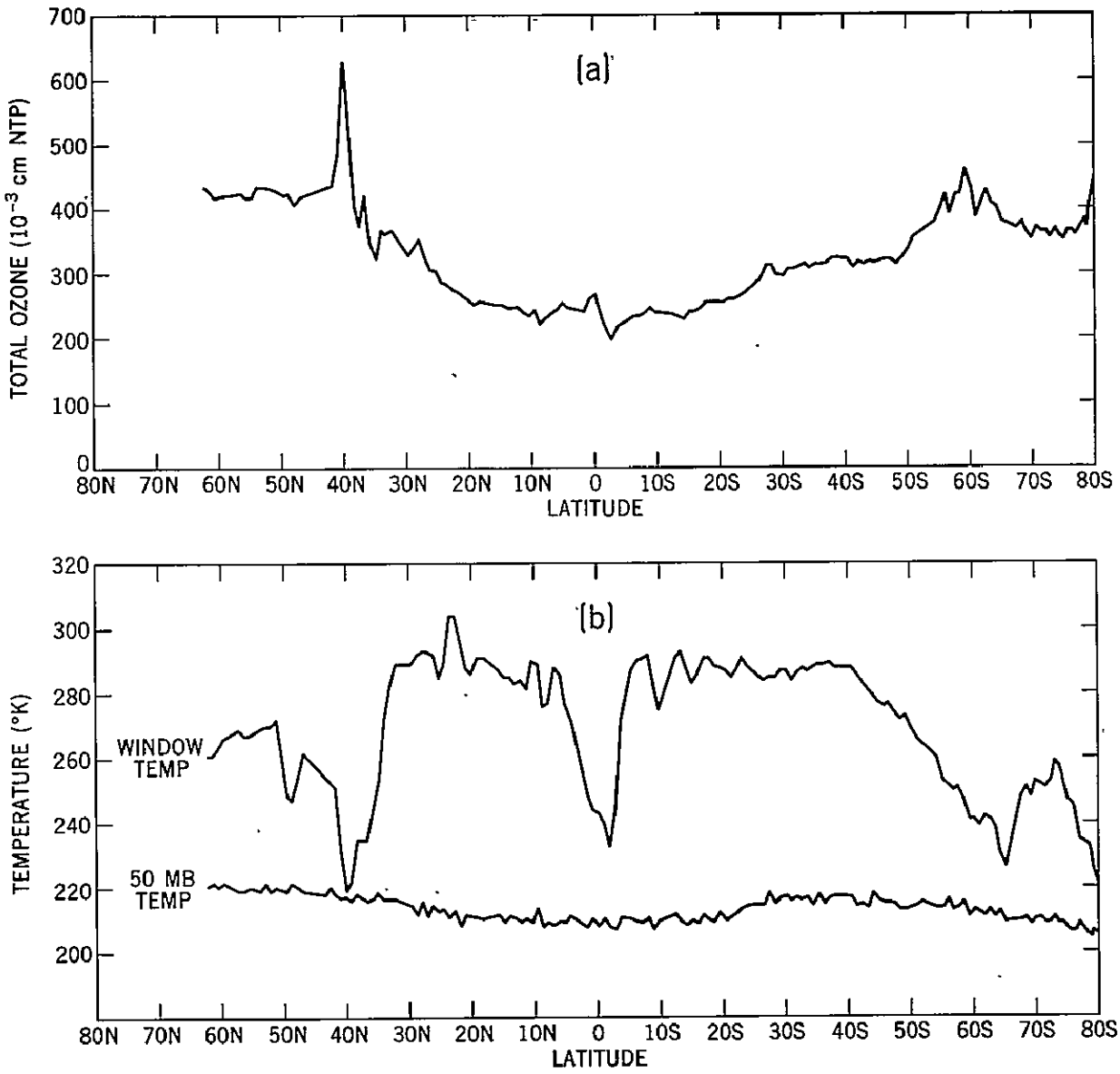

Figure 15. (a) Total ozone in an atmospheric column as a function of latitude inferred from data acquired during approximately one half of one orbit on April 22, 1969. (b) Atmospheric temperatures at 50 mb and atmospheric "window" brightness temperatures for the same pass. The 50 mb temperatures were obtained from temperature profile estimates, using measurements in the 667 cm^{-1} CO_2 band.

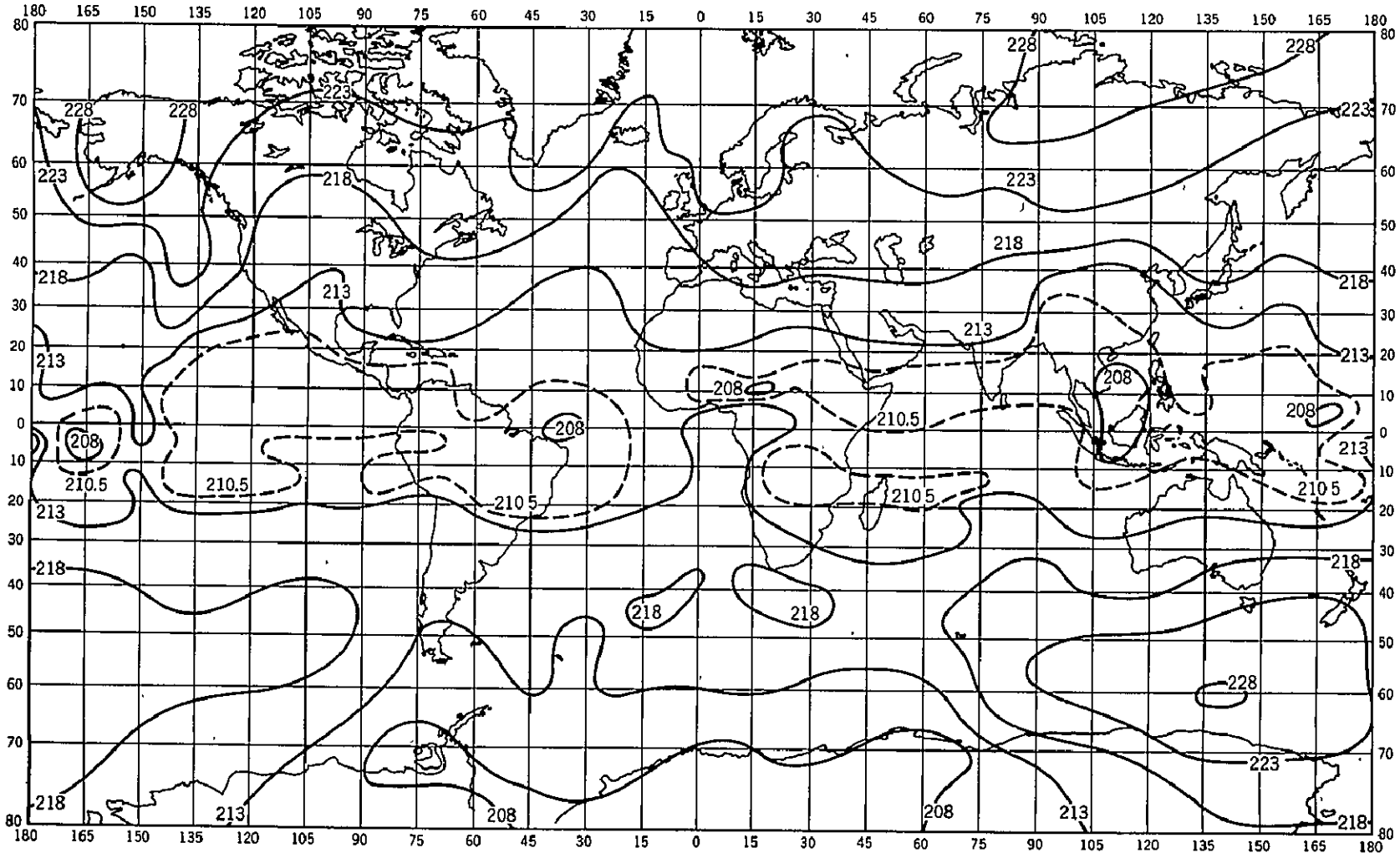

Figure 16a. Global distribution of temperatures in degrees Kelvin at the 50 mb level inferred from the satellite data. The map is based on data aquired over a 24-hour period on April 22, 1969.

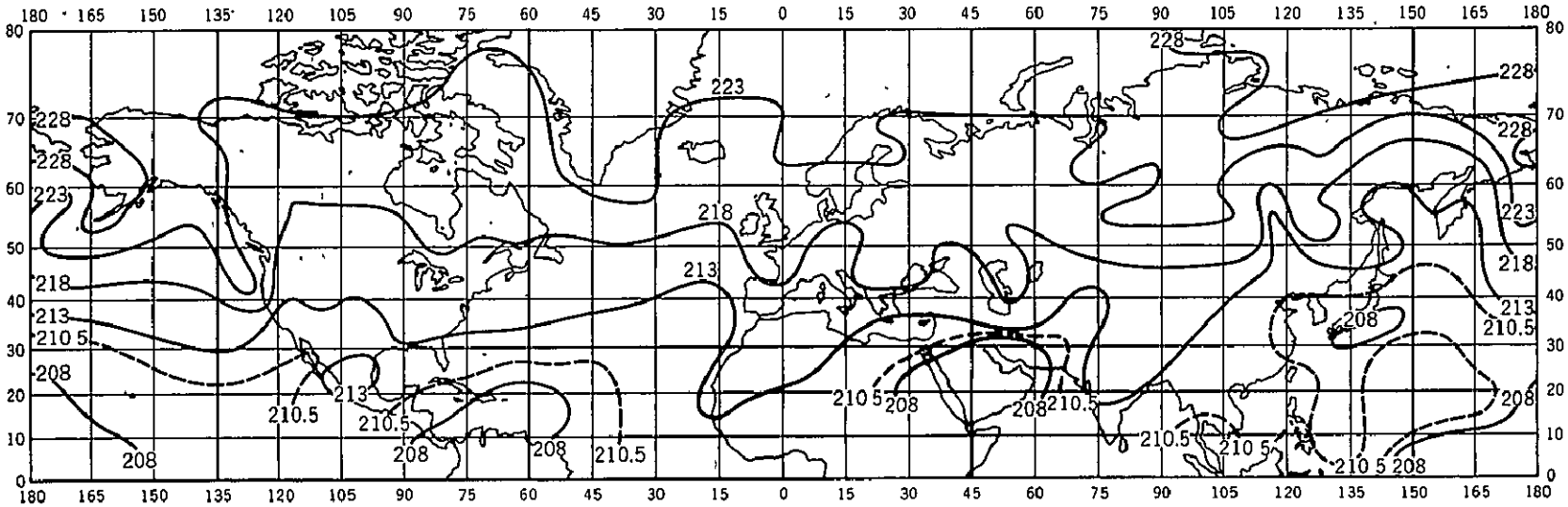

Figure 16b. · Northern Hemisphere distribution of 50 mb temperatures based on conventional radiosonde data taken at 1200 GMT on April 22, 1969.

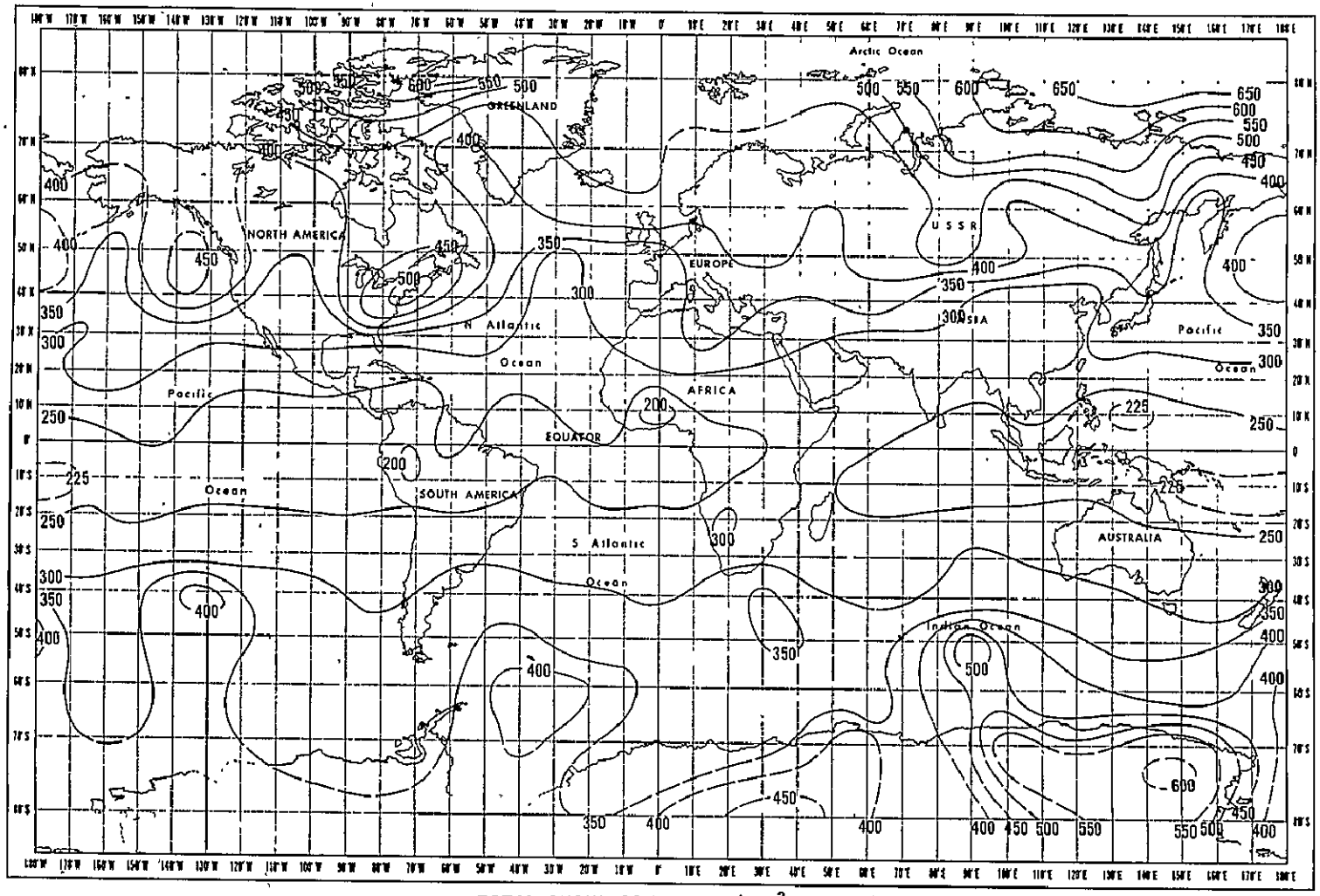

TOTAL OZONE CONTENT (10^{-3} CM STP)
APRIL 22, 1969

Figure 17. Global map of total ozone in an atmospheric column derived from measurements in the 1042 cm^{-1} band. The map is based on data acquired during a 24-hour period on April 22, 1969. The units employed are 10^{-3} cm NTP.

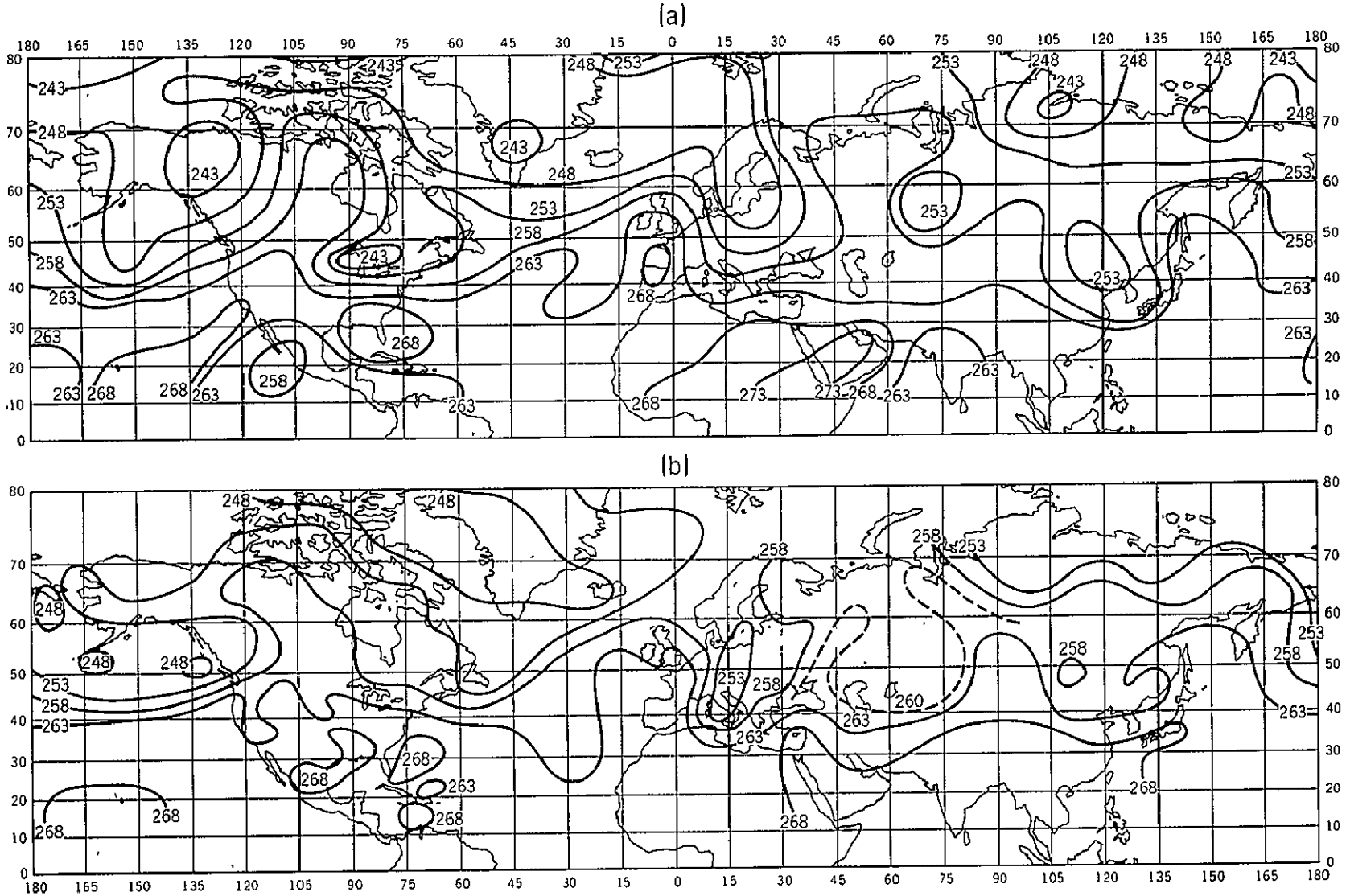

Figure 18. (a) Distribution of temperature in the Northern Hemisphere for the 500 mb level obtained from satellite data over a 24-hour period on July 11, 1969. (b) Distribution of temperature in the Nothern Hemisphere for the 500 mb level based on radiosonde data acquired at 1200 GMT on July 11, 1969.

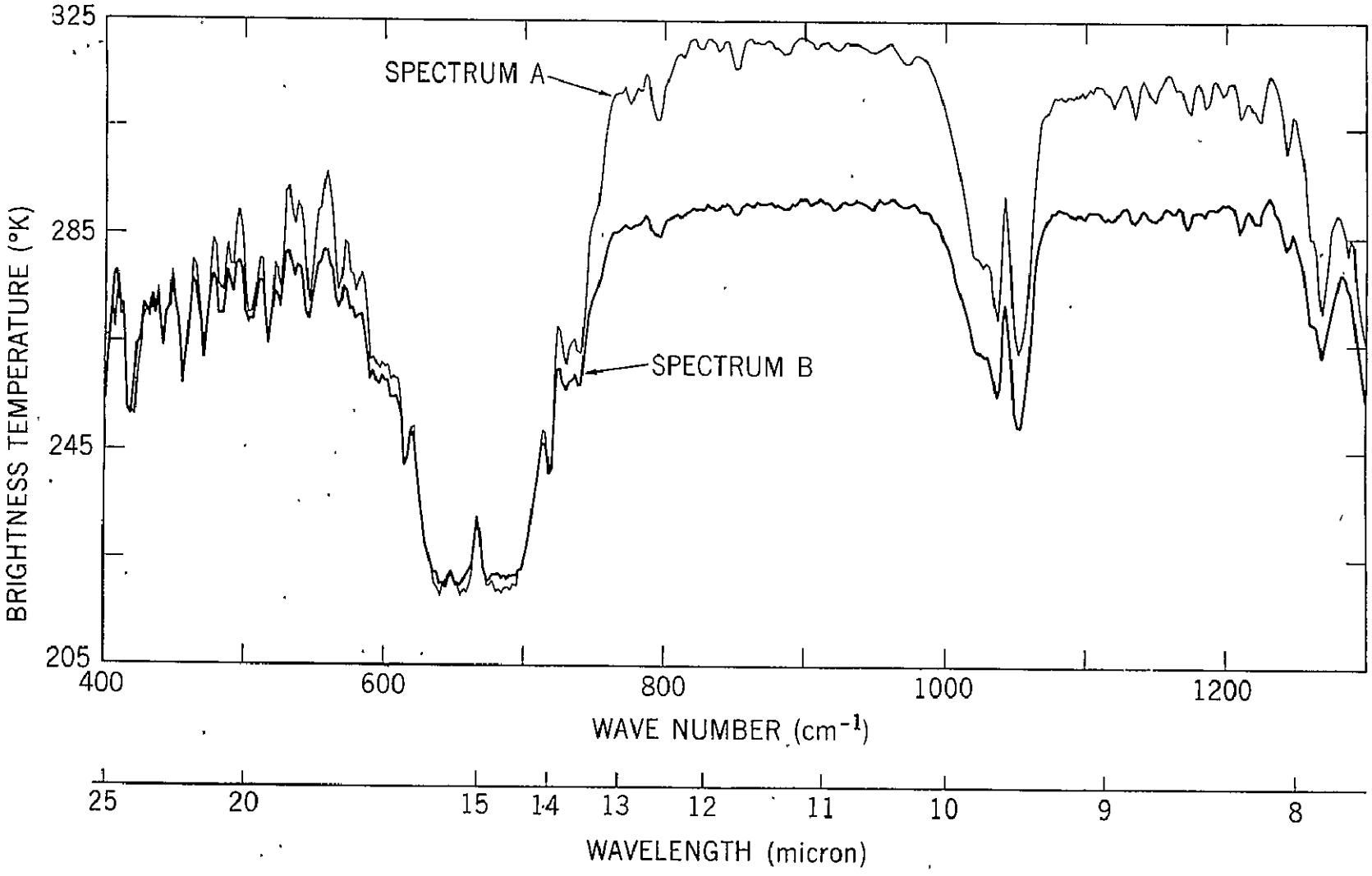

Figure 19. Spectra illustrating the effects of the reststrahlen phenomenon acquired (a) over southern Egypt and (b) over the Mediterranean Sea. The spectra are expressed in terms of brightness temperature. Spectrum (a) shows lower brightness temperatures in the window region on the high wave number side of the 1042 cm^{-1} ozone band compared with the window region on the low wave number side while spectrum (b) shows essentially the same brightness temperatures on either side of the ozone band.